

A polarized discrete ordinate scattering model for simulations of limb and nadir long-wave measurements in 1-D/3-D spherical atmospheres

C. Emde,¹ S. A. Buehler,¹ C. Davis,² P. Eriksson,³ T. R. Sreerekha,¹ and C. Teichmann¹

Received 17 June 2004; revised 29 September 2004; accepted 7 October 2004; published 21 December 2004.

[1] This article describes one of the scattering algorithms of the three-dimensional polarized radiative transfer model ARTS (Atmospheric Radiative Transfer Simulator) which has been implemented to study for example the influence of cirrus clouds on microwave limb sounding. The model uses the DOIT (Discrete Ordinate Iterative) method to solve the vector radiative transfer equation. The implementation of a discrete ordinate method is challenging due to the spherical geometry of the model atmosphere which is required for the simulation of limb radiances. The involved numerical issues, which are grid optimization and interpolation methods, are discussed in this paper. Scattering simulations are presented for limb- and down-looking geometries, for one-dimensional and three-dimensional spherical atmospheres. They show the impact of cloud particle size, shape, and orientation on the brightness temperatures and on the polarization of microwave radiation in the atmosphere. The cloud effect is much larger for limb radiances than for nadir radiances. Particle size is a very important parameter in all simulations. The polarization signal is negligible for simulations with completely randomly oriented particles, whereas for horizontally aligned particles with random azimuthal orientation the polarization signal is significant. Moreover, the effect of particle shape is only relevant for oriented cloud particles. The simulations show that it is essential to use a three-dimensional scattering model for inhomogeneous cloud layers. *INDEX TERMS:* 0320

Atmospheric Composition and Structure: Cloud physics and chemistry; 0340 Atmospheric Composition and Structure: Middle atmosphere—composition and chemistry; 0360 Atmospheric Composition and Structure: Transmission and scattering of radiation; 3210 Mathematical Geophysics: Modeling; *KEYWORDS:* radiative transfer, cirrus clouds, microwave

Citation: Emde, C., S. A. Buehler, C. Davis, P. Eriksson, T. R. Sreerekha, and C. Teichmann (2004), A polarized discrete ordinate scattering model for simulations of limb and nadir long-wave measurements in 1-D/3-D spherical atmospheres, *J. Geophys. Res.*, *109*, D24207, doi:10.1029/2004JD005140.

1. Introduction

[2] Millimeter-wave limb sounding is a well established technique for the observation of atmospheric trace gases in the stratosphere and upper troposphere. Two instruments of this type are the Earth Observing System Microwave Limb Sounder (EOS MLS) [Waters *et al.*, 1999] and the Millimeter Atmospheric Sounder (MAS) [Hartmann *et al.*, 1996]. Recently, instruments have moved toward higher frequencies into the submillimeter-wave region; examples of this type of instrument are Odin-SMR [Murtagh *et al.*,

2002] and the Superconduction Submillimeter-Wave Limb Emission Sounder (SMILES) (S. A. Buehler *et al.*, Expected performance of the SMILES Submillimeter-Wave Limb Sounder compared to aircraft data, submitted to *Radio Science*, 2004). Clouds, especially cirrus, with particle sizes exceeding microwave wavelengths, can severely disturb trace gas measurements. On the other hand, it is possible to obtain cloud information from microwave limb radiances affected by cirrus clouds. This requires a radiative transfer model that can simulate the scattering effect of cirrus clouds.

[3] A number of well established radiative transfer models exist for the clear-sky case, notably the public domain Atmospheric Radiative Transfer Simulator (ARTS) [Buehler *et al.*, 2005], which was taken as the platform for the new scattering model described here. The model development is a challenging task for various reasons: Firstly, cloud coverage is vertically and horizontally inhomogeneous which implies that a three-dimensional (3-D) model is unavoidable for the simulation of realistic cases. Especially for limb measurements, the 3-D spherical geometry is required as the

¹Institute of Environmental Physics, University of Bremen, Bremen, Germany.

²Institute for Atmospheric and Environmental Science, University of Edinburgh, Edinburgh, UK.

³Department of Radio and Space Science, Chalmers University of Technology, Göteborg, Sweden.

observed region in the atmosphere has a horizontally large extent. Secondly, cirrus clouds consist of particles of different sizes and shapes. As particle scattering due to nonspherical particles leads to polarization effects [Czekala and Simmer, 1998] the vector radiative transfer equation (VRTE) has to be used in the model to obtain the full Stokes vector, not just the intensity of the radiation.

[4] Liquid water clouds are not so problematic, because liquid water drops mainly act as absorbers, not as scatterers. Cirrus clouds, on the other hand, have a low absorption coefficient [see, e.g., Mishchenko *et al.*, 2002] and a rather large scattering coefficient. Aerosol scattering needs to be considered in the infra-red. Molecular Rayleigh scattering, though important for optical wavelength, can be neglected at microwave and infra-red wavelengths.

[5] A survey of existing freely available radiative transfer models yielded none that were well-suited to the requirements described above. For instance, the 3-D Monte Carlo models described in Liu *et al.* [1996] and Roberti *et al.* [1994] are only applicable for macroscopically isotropic and mirror-symmetric scattering media, where polarization effects can be neglected. The 3-D discrete ordinate models SHDOM [Evans, 1998] and VDOM [Haferman *et al.*, 1997] assume a cartesian geometry and are for this reason not applicable for limb simulations. Other discrete ordinate models, for example, MWMOD [Simmer, 1993] and VDISORT [Schulz and Stammes, 2000], use one-dimensional (1-D) plane-parallel geometries. Another well known method is the Eddington approximation [e.g., Kummerow, 1993], which is also not well-suited to the limb sounding problem, as it is only valid in plane-parallel atmospheres. A simple 1-D plane-parallel model using a prototype of the iterative solution method described in this article is described in Sreerekha *et al.* [2002].

[6] In the new version of ARTS two scattering methods have been implemented: a backward Monte Carlo Method [Davis *et al.*, 2004] and the DOIT (Discrete Ordinate Iterative) method being presented in this paper. Both methods work in 3-D spherical atmospheres and both can simulate polarization effects due to aspherical particles. The DOIT method works also in 1-D spherical atmospheres. The implementation of the DOIT method is very similar to discrete ordinate method (DOM) implementations for instance in SHDOM or VDOM. The originality of the DOIT method is, that the DOM has been adapted to a spherical geometry, which is essential for the simulation of limb radiances. The model can be applied in the microwave and in the infrared. The 1-D version of the DOIT method was used to simulate the effect of different cloud parameters on limb spectra [Emde *et al.*, 2004]. It was compared to a model developed at RAL (Rutherford Appelton Laboratory) [Kerridge *et al.*, 2003] and the single scattering model KOPRA developed for MIPAS (Michelson Interferometer for Passive Atmospheric Sounding) [Hoepfner and Emde, 2005]. ARTS-DOIT and the RAL model showed excellent agreement (less than 1K difference in simulated brightness temperatures for most cloud cases) and ARTS-DOIT and KOPRA agreed well in the single scattering regime. KOPRA as well as the RAL model neglect polarization. KOPRA only works for 1-D spherical atmospheres, whereas the RAL model works in 1-D and 2-D pseudo-spherical atmospheres. The two models run faster than the

ARTS model, but ARTS is the more general and more accurate model.

[7] The Monte Carlo method and the DOIT method will eventually be compared. The results of this comparison will be published separately.

[8] Section 2 of this paper generally describes microwave radiative transfer with scattering and defines the notations used in the later sections. In section 3 the DOIT method is explained. The atmospheric setup used in all presented examples is given in section 4. Section 5 identifies numerical problems and presents the solutions as implemented in ARTS. Furthermore it gives accuracy estimates of the simulations. Section 6 presents simulations for a 1-D atmosphere which show the effect of particle size and shape on the intensity of the radiation and on the polarization signal. To demonstrate inhomogeneity effect and the importance of a 3-D model, 3-D scattering simulations are presented in section 7.

2. Radiative Transfer Equation

[9] The vector radiative transfer equation (VRTE) for a medium with thermal emission including sparsely and randomly distributed, arbitrarily oriented particles is according to [Mishchenko *et al.*, 2002]:

$$\frac{d\mathbf{I}}{ds}(\mathbf{n}, \nu, T) = -\langle \mathbf{K}(\mathbf{n}, \nu, T) \rangle \mathbf{I}(\mathbf{n}, \nu, T) + \langle \mathbf{a}(\mathbf{n}, \nu, T) \rangle B(\nu, T) + \int_{4\pi} d\mathbf{n}' \langle \mathbf{Z}(\mathbf{n}, \mathbf{n}', \nu, T) \rangle \mathbf{I}(\mathbf{n}', \nu, T) \quad (1)$$

where \mathbf{I} is the Stokes vector, $\langle \mathbf{K} \rangle$ the ensemble-averaged extinction matrix, $\langle \mathbf{a} \rangle$ the ensemble-averaged absorption vector, B the Planck function and $\langle \mathbf{Z} \rangle$ the ensemble-averaged phase matrix. Furthermore ν is the frequency of the radiation, T is the temperature, ds is a path-length-element of the propagation path and \mathbf{n} the propagation direction. Equation (1) is valid for monochromatic radiative transfer. We can use this equation for simulating microwave radiative transfer through the atmosphere, as the scattering events do not change the frequency of the radiation.

[10] The four-component Stokes vector $\mathbf{I} = (I, Q, U, V)^T$ fully describes the radiation and it can directly be associated with the measurements carried out by a radiometer used for remote sensing. The first component I is the intensity of the radiation. The other components describe the polarization state of the radiation. Q describes the linear polarization; it is the difference between the intensities of the horizontally polarized and the vertically polarized part of the radiation. U is also related to linear polarization, and V describes the circular polarization [see Bohren and Huffman, 1998].

[11] The optical properties $\langle \mathbf{K} \rangle$, $\langle \mathbf{a} \rangle$ and $\langle \mathbf{Z} \rangle$ are averaged over all particle types and orientations. The total gas absorption is also included in $\langle \mathbf{K} \rangle$ and $\langle \mathbf{a} \rangle$. The averaging is described in detail in Eriksson *et al.* [2004].

[12] The scalar radiative transfer equation (SRTE)

$$\frac{dI}{ds}(\mathbf{n}, \nu, T) = -\langle K_{11}(\mathbf{n}, \nu, T) \rangle I(\mathbf{n}, \nu, T) + \langle a_1(\mathbf{n}, \nu, T) \rangle B(\nu, T) + \int_{4\pi} d\mathbf{n}' \langle Z_{11}(\mathbf{n}, \mathbf{n}', \nu, T) \rangle I(\mathbf{n}', \nu, T) \quad (2)$$

can be used presuming that the radiation field is unpolarized. This assumption is reasonable if the scattering medium consists of spherical or completely randomly oriented particles, where $\langle \mathbf{K}^p \rangle$ is diagonal and only the first element of $\langle \mathbf{a}^p \rangle$ is nonzero.

3. Discrete Ordinate Iterative Method

3.1. Basic Definitions

[13] Cloudbox: It is not necessary to solve the scattering problem in the whole atmosphere. ARTS allows the definition of a region called the “cloudbox,” in which cloud particles may exist, by specifying pressure (p), latitude (α) and longitude (β) limits. In order to save computation time and memory, the scattering problem is only solved inside the cloudbox.

[14] Radiation field: The Stokes vector depends on the position in the cloudbox and on the propagation direction specified by the zenith angle (θ) and the azimuth angle (ϕ). All these dimensions are discretized inside the model; five numerical grids are required to represent the radiation field \mathcal{I} :

$$\begin{aligned} \vec{p} &= \{p_1, p_2, \dots, p_{N_p}\} \\ \vec{\alpha} &= \{\alpha_1, \alpha_2, \dots, \alpha_{N_\alpha}\} \\ \vec{\beta} &= \{\beta_1, \beta_2, \dots, \beta_{N_\beta}\} \\ \vec{\theta} &= \{\theta_1, \theta_2, \dots, \theta_{N_\theta}\} \\ \vec{\phi} &= \{\phi_1, \phi_2, \dots, \phi_{N_\phi}\} \end{aligned} \quad (3)$$

The radiation field is a set of Stokes vectors ($N_p \times N_\alpha \times N_\beta \times N_\theta \times N_\phi$ elements) for all combinations of positions and directions:

$$\mathcal{I} = \left\{ \mathbf{I}_1(p_1, \alpha_1, \beta_1, \theta_1, \phi_1), \mathbf{I}_2(p_2, \alpha_1, \beta_1, \theta_1, \phi_1), \dots, \mathbf{I}_{N_p \times N_\alpha \times N_\beta \times N_\theta \times N_\phi}(p_{N_p}, \alpha_{N_\alpha}, \beta_{N_\beta}, \theta_{N_\theta}, \phi_{N_\phi}) \right\} \quad (4)$$

In the following we will use the notation

$$\begin{aligned} i &= 1 \dots N_p \\ j &= 1 \dots N_\alpha \\ \mathcal{I} &= \{ \mathbf{I}_{ijklm} \} & k &= 1 \dots N_\beta \\ l &= 1 \dots N_\theta \\ m &= 1 \dots N_\phi \end{aligned} \quad (5)$$

3.2. Vector Radiative Transfer Equation Solution

[15] The first guess field

$$\mathcal{I}^{(0)} = \{ \mathbf{I}_{ijklm}^{(0)} \} \quad (6)$$

is partly determined by the boundary condition given by the radiation coming from the clear-sky part of the atmosphere traveling into the cloudbox. Inside the cloudbox an arbitrary field can be chosen as a first guess. In order to minimize the

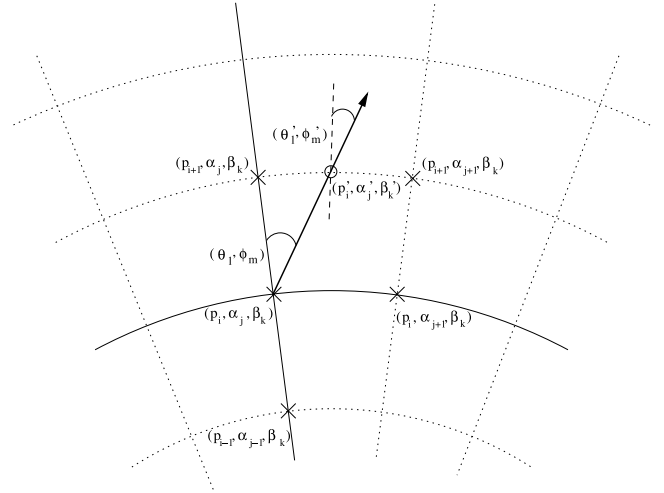


Figure 1. Path from a grid point ($(p_i, \alpha_j, \beta_k) - (\times)$) to the intersection point ($(p'_i, \alpha'_j, \beta'_k) - (\circ)$) with the next grid cell boundary. Viewing direction is specified by (θ_i, ϕ_m) at (\times) or (θ'_i, ϕ'_m) at (\circ) .

number of iterations it should be as close as possible to the solution field.

[16] The next step is to solve the scattering integrals

$$\langle \mathbf{S}_{ijklm}^{(0)} \rangle = \int_{4\pi} d\mathbf{n}' \langle \mathbf{Z}_{ijklm} \rangle \mathbf{I}_{ijklm}^{(0)} \quad (7)$$

using the first guess field. For the integration we use equidistant angular grids in order to save computation time (see section 5.2). The radiation field which is generally defined on finer angular grids ($\vec{\phi}, \vec{\theta}$) is interpolated on the equidistant angular grids. The integration is performed over all incident directions \mathbf{n}' for each propagation direction \mathbf{n} . The evaluation of the scattering integral is done for all grid points inside the cloudbox. The obtained integrals are interpolated on $\vec{\phi}$ and $\vec{\theta}$. The result is the first guess scattered field $\mathcal{S}^{(0)}$:

$$\mathcal{S}^{(0)} = \{ \langle \mathbf{S}_{ijklm}^{(0)} \rangle \} \quad (8)$$

[17] Figure 1 shows a propagation path step from a grid point $\mathbf{P} = (p_i, \alpha_j, \beta_k)$ into direction $\mathbf{n} = (\theta_i, \phi_m)$. The radiation arriving at \mathbf{P} from the direction \mathbf{n}' is obtained by solving the linear differential equation:

$$\frac{d\mathbf{I}^{(1)}}{ds} = -\overline{\langle \mathbf{K} \rangle} \mathbf{I}^{(1)} + \overline{\langle \mathbf{a} \rangle} \overline{\mathcal{B}} + \overline{\langle \mathbf{S}^{(0)} \rangle} \quad (9)$$

where $\overline{\langle \mathbf{K} \rangle}$, $\overline{\langle \mathbf{a} \rangle}$, $\overline{\mathcal{B}}$ and $\overline{\langle \mathbf{S}^{(0)} \rangle}$ are averaged quantities. This equation can be solved analytically for constant coefficients. Multilinear interpolation gives the quantities \mathbf{K}' , \mathbf{a}' , \mathbf{S}' and T' at the intersection point \mathbf{P}' . To calculate the radiative transfer from \mathbf{P}' toward \mathbf{P} , all quantities are approximated by taking the averages between the values at \mathbf{P}' and \mathbf{P} . The

average value of the temperature is used to get the averaged Planck function \overline{B} .

[18] The solution of equation (9) is found analytically using a matrix exponential approach (see Appendix A):

$$\mathbf{I}^{(1)} = e^{-\overline{(\mathbf{K})}s} \mathbf{I}^{(0)} + \left(\mathbf{1} - e^{-\overline{(\mathbf{K})}s} \right) \overline{(\mathbf{K})}^{-1} \left(\overline{(\mathbf{a})} \overline{B} + \overline{(\mathbf{S}^{(0)})} \right) \quad (10)$$

where $\mathbf{1}$ denotes the identity matrix and $\mathbf{I}^{(0)}$ the initial Stokes vector. The radiative transfer step from \mathbf{P}' to \mathbf{P} is calculated, therefore $\mathbf{I}^{(0)}$ is the incoming radiation at \mathbf{P}' into direction (θ'_l, ϕ'_m) , which is the first guess field interpolated on \mathbf{P}' . This radiative transfer step calculation is done for all points inside the cloudbox in all directions. The resulting set of Stokes vectors ($\mathbf{I}^{(1)}$ for all points in all directions) is the first order iteration field $\mathcal{I}^{(1)}$:

$$\mathcal{I}^{(1)} = \left\{ \mathbf{I}_{ijklm}^{(1)} \right\} \quad (11)$$

[19] We can formulate a differential equation for the n -th order iteration field. The scattering integrals are given by

$$\langle \mathbf{S}_{ijklm}^{(n-1)} \rangle = \int_{4\pi} d\mathbf{n}' \langle \mathbf{Z} \rangle \mathbf{I}_{ijklm}^{(n-1)} \quad (12)$$

and the differential equation for a specified grid point into a specified direction is

$$\frac{d\mathbf{I}^{(n)}}{ds} = -\overline{(\mathbf{K})} \mathbf{I}^{(n)} + \overline{(\mathbf{a})} \overline{B} + \overline{(\mathbf{S}^{(n-1)})}. \quad (13)$$

Thus the n -th order iteration field

$$\mathcal{I}^{(n)} = \left\{ \mathbf{I}_{ijklm}^{(n)} \right\} \quad (14)$$

is given by

$$\mathbf{I}^{(n)} = e^{-\overline{(\mathbf{K})}s} \cdot \mathbf{I}^{(n-1)} + \left(\mathbf{1} - e^{-\overline{(\mathbf{K})}s} \right) \overline{(\mathbf{K})}^{-1} \left(\overline{(\mathbf{a})} \overline{B} + \overline{(\mathbf{S}^{(n-1)})} \right) \quad (15)$$

for all cloudbox points and all directions defined in the numerical grids.

[20] After each iteration a convergence test is performed. If the absolute difference for all successive Stokes vectors

$$|\mathbf{I}_{ijklm}^{(N)} - \mathbf{I}_{ijklm}^{(N-1)}| < \epsilon \quad (16)$$

a solution to the vector radiative transfer equation (1) has been found:

$$\mathcal{I}^{(N)} = \left\{ \mathbf{I}_{ijklm}^{(N)} \right\} \quad (17)$$

3.3. Scalar Radiative Transfer Equation Solution

[21] In analogy to the scattering integral vector field the scalar scattering integral field is obtained:

$$\langle S_{ijklm}^{(0)} \rangle = \int_{4\pi} d\mathbf{n}' \langle Z_{11} \rangle I_{ijklm}^{(0)} \quad (18)$$

The scalar radiative transfer equation (2) with fixed scattering integral is

$$\frac{dI^{(1)}}{ds} = -\langle K_{11} \rangle I^{(1)} + \langle a_1 \rangle B + \langle S^{(0)} \rangle. \quad (19)$$

Assuming constant coefficients, this equation is solved analytically after averaging extinction coefficient, absorption coefficient, scattering vector, and the temperature. The averaging procedure is done analogously to the procedure described for solving the VRTE. The solution of the averaged differential equation is

$$I^{(1)} = I^{(0)} e^{-\overline{(\mathbf{K}_{11})}s} + \frac{\langle a_1 \rangle \overline{B} + \langle S^{(0)} \rangle}{\overline{(\mathbf{K}_{11})}} \left(1 - e^{-\overline{(\mathbf{K}_{11})}s} \right) \quad (20)$$

where $I^{(0)}$ is obtained by interpolating the initial field. $\overline{(\mathbf{K}_{11})}$, $\langle a_1 \rangle$, \overline{B} and $\langle S^{(0)} \rangle$ are the averaged values for extinction coefficient, absorption coefficient, Planck function and the scattering integral respectively. Applying this equation leads to the first iteration scalar intensity field, consisting of the intensities $I^{(1)}$ at all points in the cloudbox for all directions.

[22] As the solution to the vector radiative transfer equation the solution to the scalar radiative transfer equation is found numerically by the same iterative method. The convergence test for the scalar equation compares the values of the calculated intensities of two successive iteration fields.

3.4. Single Scattering Approximation

[23] The DOIT method uses the single scattering approximation for one propagation path step. It is possible to choose a rather coarse grid inside the cloudbox. The user can define a limit for the maximum propagation path step length. If a propagation path step from one grid cell to the intersection point with the next grid cell boundary is greater than this value, the path step is divided in several steps such that all steps are less than the maximum value. In our calculations the optical depth due to cloud particles for one propagation path substep was in all cases less than 0.01, which is sufficiently small to assume single scattering. The radiative transfer calculation is done along this propagation path through one grid cell. All coefficients of the VRTE and the Stokes vector fields are interpolated linearly on the propagation path points.

3.5. Clear-Sky Radiative Transfer

[24] Usually one wants to simulate measurements, for instance satellite measurements. To obtain the signal for a sensor located at an altitude of about 800 km which is far away from the cloudbox, the scattering signal needs to be propagated from the cloudbox toward the sensor through the clear-sky atmosphere above the clouds. The clear-sky part of the ARTS model is used to calculate this part. The

interface between the scattering calculation and the clear-sky calculation is the cloudbox boundary. To simulate a satellite measurement, the line of sight (LOS) of the instrument is calculated. The radiation field on the cloudbox-boundary, which is obtained by using the DOIT method or the Monte Carlo method, is taken as radiative background for a clear-sky calculation from the cloudbox toward the sensor, if the LOS intersects with the cloudbox. Clear-sky calculations are also necessary to obtain the boundary condition for the DOIT method, that is the clear-sky radiation field on the cloudbox boundary. For detailed descriptions of the clear-sky calculations and the sensor modeling refer to *Eriksson et al.* [2004].

4. Definition of Clouds and Atmospheric Fields

[25] In the Earth's atmosphere we find liquid water clouds consisting of approximately spherical water droplets and cirrus clouds consisting of ice particles of diverse shapes and sizes. We also find different kinds of aerosols. In order to take into account this variety, the model allows to define several particle types. A particle type is either a specified particle or a specified particle distribution, for example a particle ensemble following a gamma size distribution. The particles can be completely randomly oriented, azimuthally randomly oriented or arbitrarily oriented. For each particle type being a part of the modeled cloud field, a data file containing the single scattering properties ($\langle \mathbf{K} \rangle$, $\langle \mathbf{a} \rangle$, and $\langle \mathbf{Z} \rangle$), and the appropriate particle number density field is required. The particle number density fields are stored in data files, which include the field stored in a three-dimensional array and also the appropriate atmospheric grids (pressure, latitude and longitude grid). For each grid point in the cloudbox the single scattering properties are averaged using the particle number density fields. In the scattering database the single scattering properties are not always stored in the atmospheric coordinate system. For instance for randomly oriented particles it makes sense to store the single scattering properties in the particle frame in order to reduce memory requirements (refer to Appendix B for more details).

[26] The atmospheric fields, which are temperature, altitude, and volume mixing ratio fields, are stored in the same format as the particle number density fields.

5. Numerical Issues

[27] The high dimensionality of the scattering problem complicates the development of an accurate and time-efficient solution algorithm. In this work we have focussed on accuracy, but several efficiency optimizations were necessary. Some of these efficiency measures are described in this section.

5.1. Sequential Update of the Intensity Field

[28] In section 3 the iterative solution method for the VRTE has been described. For each grid point inside the cloudbox the intersection point with the next grid cell boundary is determined in each viewing direction. After that all the quantities involved in the VRTE are interpolated onto this intersection point. As described in the sections above, the intensity field of the previous iteration is taken to

obtain the Stokes vector at the intersection point. Suppose that there are N pressure levels inside the cloudbox. If the radiation field is updated taking into account for each grid point only the adjacent grid cells, at least $N-1$ iterations are required until the scattering effect from the lower-most pressure level has propagated throughout the cloudbox up to the uppermost pressure level. From these considerations, it follows, that the number of iterations depends on the number of grid points inside the cloudbox. This means that the original method is very ineffective where a fine resolution inside the cloudbox is required to resolve the cloud inhomogeneities.

[29] A solution to this problem is the "sequential update of the radiation field," which is shown schematically in Figure 2. For simplicity it will be explained in detail for a 1-D cloudbox. We divide the update of the radiation field, i.e., the radiative transfer step calculations for all positions and directions inside the cloudbox, into three parts: Update for "up-looking" zenith angles ($0^\circ \leq \theta_{up} \leq 90^\circ$), for "down-looking" angles ($\theta_{limit} \leq \theta_{down} \leq 180^\circ$) and for "limb-looking" angles ($90^\circ < \theta_{limb} < \theta_{limit}$). The "limb-looking" case is needed, because for angles between 90° and θ_{limit} the intersection point is at the same pressure level as the observation point. The limiting angle θ_{limit} is calculated geometrically. Note that the propagation direction of the radiation is opposite to the viewing direction or LOS-direction, which is indicated by the arrows. In the 1-D case the radiation field is a set of Stokes vectors each of which depend upon the position and direction:

$$\mathcal{I} = \{\mathbf{I}(p_i, \theta_l)\} \quad (21)$$

[30] The boundary condition for the calculation is the incoming radiation field on the cloudbox boundary \mathcal{I}^{bd} :

$$\mathcal{I}^{bd} = \{\mathbf{I}(p_i, \theta_l)\} \quad \text{where} \quad \begin{aligned} p_i &= p_N \quad \forall \quad \theta_l \in [0, \theta_{limit}] \\ p_i &= p_0 \quad \forall \quad \theta_l \in (\theta_{limit}, 180^\circ] \end{aligned} \quad (22)$$

Here p_0 and p_N are the pressure coordinates of the lower and upper cloudbox boundaries respectively. For down-looking directions, the intensity field at the lower-most cloudbox boundary and for up- and limb-looking directions the intensity field at the uppermost cloudbox boundary are the required boundary conditions, respectively.

[31] Up-looking directions: In this part of the sequential update the downwelling radiation is considered. The first step of the sequential update is to calculate the intensity field for the pressure coordinate p_{N-1} , the pressure level below the uppermost boundary, for all up-looking directions. Radiative transfer steps are calculated for paths starting at the uppermost boundary and propagating to the $(N-1)$ pressure level. The required input for this radiative transfer step are the averaged coefficients of the uppermost cloudbox layer and the Stokes vectors at the uppermost boundary for all up-looking directions. These are obtained by interpolating the boundary condition \mathcal{I}^{bd} on the appropriate zenith angles. Note that the zenith angle of the propagation path for the observing direction θ_l does not equal θ_l' at the intersection point due to the spherical

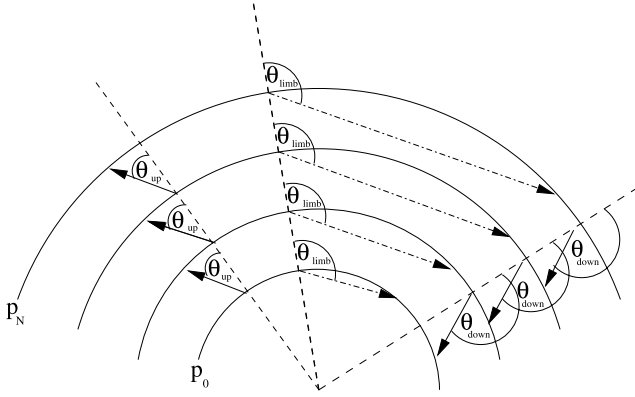


Figure 2. Schematic of the sequential update (1-D) showing the three different parts: “up-looking” corresponds to zenith angles θ_{up} , “limb-looking” corresponds to θ_{limb} , and “down-looking” corresponds to θ_{down} .

geometry. If θ_l is close to 90° this difference is most significant.

[32] To calculate the intensity field for the pressure coordinate p_{N-2} , we repeat the calculation above. We have to calculate a radiative transfer step from the $(N-1)$ to the $(N-2)$ pressure level. As input we need the interpolated intensity field at the $(N-1)$ pressure level, which has been calculated in the last step.

[33] For each pressure level $(m-1)$ we take the interpolated field of the layer above ($\mathcal{I}(p_m)^{(1)}$). Using this method, the scattering influence from the particles in the upper-most cloudbox layer can propagate during one iteration down to the lower-most layer. This means that the number of iterations does not scale with the number of pressure levels, which would be the case without sequential update.

[34] The radiation field at a specific point in the cloudbox is obtained by solving equation (10). For up-looking directions at position p_{m-1} we may write:

$$\begin{aligned} \mathbf{I}(p_{m-1}, \theta_{up})^{(1)} &= e^{-\overline{\langle \mathbf{K}(\theta_{up}) \rangle s}} \mathbf{I}(p_m, \theta_{up})^{(1)} \\ &+ \left(1 - e^{-\overline{\langle \mathbf{K}(\theta_{up}) \rangle s}} \right) \overline{\langle \mathbf{K}(\theta_{up}) \rangle}^{-1} \\ &\times \left(\overline{\langle \mathbf{a}(\theta_{up}) \rangle \overline{\mathbf{B}}} + \overline{\langle \mathbf{S}(\theta_{up})^{(0)} \rangle} \right) \end{aligned} \quad (23)$$

For simplification we write

$$\mathbf{I}(p_{m-1}, \theta_{up})^{(1)} = \mathbf{A}(\theta_{up}) \mathbf{I}(p_m, \theta_{up})^{(1)} + \mathbf{B}(\theta_{up}) \quad (24)$$

Solving this equation sequentially, starting at the top of the cloud and finishing at the bottom, we get the updated radiation field for all up-looking angles.

$$\mathcal{I}(p_i, \theta_{up})^{(1)} = \left\{ \mathbf{I}^{(1)}(p_i, \theta_l) \right\} \quad \forall \theta_l \in [0, 90^\circ] \quad (25)$$

[35] Down-looking directions: The same procedure is done for down-looking directions, for which we have to consider the up-welling radiation. The only difference is that the starting point is the lower-most pressure level p_1

and the incoming clear-sky field at the lower cloudbox boundary, which is interpolated on the required zenith angles, is taken as boundary condition. The following equation is solved sequentially, starting at the bottom of the cloudbox and finishing at the top:

$$\mathbf{I}(p_m, \theta_{down})^{(1)} = \mathbf{A}(\theta_{down}) \mathbf{I}(p_{m-1}, \theta_{down})^{(1)} + \mathbf{B}(\theta_{down}) \quad (26)$$

This yields the updated radiation field for all down-looking angles.

$$\mathcal{I}(p_i, \theta_{down})^{(1)} = \left\{ \mathbf{I}^{(1)}(p_i, \theta_l) \right\} \quad \forall \theta_l \in [\theta_{limit}, 180^\circ] \quad (27)$$

[36] Limb directions: A special case for limb directions, which correspond to angles slightly above 90° had to be implemented. If the tangent point is part of the propagation path step, the intersection point is exactly at the same pressure level as the starting point. In this case the linearly interpolated clear-sky field is taken as input for the radiative transfer calculation, because we do not have an already updated field for this pressure level:

$$\mathbf{I}(p_m, \theta_{limb})^{(1)} = \mathbf{A}(\theta_{limb}) \mathbf{I}(p_m, \theta_{limb})^{(0)} + \mathbf{B}(\theta_{limb}) \quad (28)$$

By solving this equation the missing part of the updated radiation field is obtained

$$\mathcal{I}(p_i, \theta_{limb})^{(1)} = \left\{ \mathbf{I}(p_i, \theta_l) \right\} \quad \forall \theta_l \in [90^\circ, \theta_{limit}] \quad (29)$$

For all iterations the sequential update is applied. Using this method the number of iterations depends only on the optical thickness of the cloud or on the number of multiple-scattering events, not on the number of pressure levels. How the sequential update is performed in the 3-D model is described by *Eriksson et al.* [2004].

5.2. Grid Optimization and Interpolation Methods

[37] The accuracy of the DOIT method depends very much on the discretization of the zenith angle. The reason is, that the intensity field strongly increases at about $\theta = 90^\circ$. For angles below 90° (“up-looking” directions) the intensity is very small compared to angles above 90° (“down-looking” directions), because the thermal emission from the lower atmosphere and from the ground is much larger than thermal emission from trace gases in the upper atmosphere. Figure 3 shows an example intensity field as a function of zenith angle for different pressure levels inside a cloudbox, which is placed from 7.3 to 12.7 km altitude, corresponding to pressure limits of 411 hPa and 188 hPa respectively. The cloudbox includes 27 pressure levels. The frequency of the sample calculation was 318 GHz. We used a midlatitude-summer scenario and included water vapor, ozone, nitrogen and oxygen. The references for the atmospheric data are given in section 6. For simplicity we chose this 1-D setup for all sample calculations in this section. As the intensity (or the Stokes vector) at the intersection point of a propagation path is obtained by interpolation, large interpolation errors can occur for zenith angles of about 90° if the zenith angle grid discretization is too coarse. Taking a very fine equidistant zenith angle grid leads to very long computation

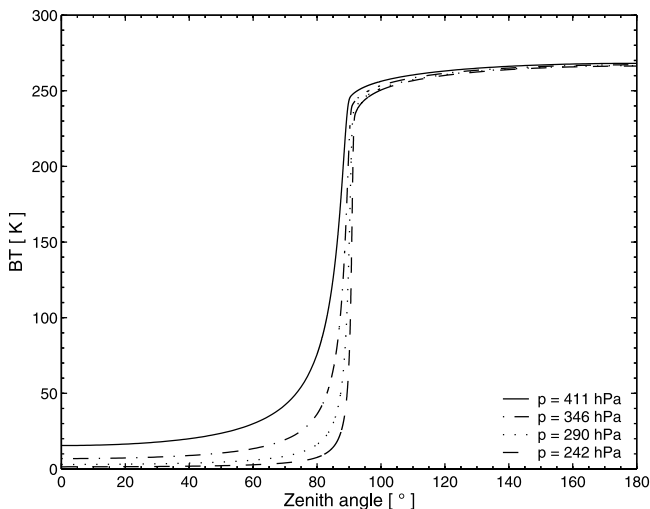


Figure 3. Intensity field for different pressure levels.

times. Therefore a zenith angle grid optimization method is required. For the computation of the scattering integral it is possible to take a much coarser zenith angle resolution without losing accuracy. It does not make sense to use the zenith angle grid, which is optimized to represent the radiation field with a certain accuracy. The integrand is the product of the phase matrix and the radiation field. The peaks of the phase matrices can be at any zenith angle, depending on the incoming and the scattered directions. The integration over the incident directions causes the scattering source function to be much smoother than the radiation field. For simplicity we have taken an equidistant zenith angle grid and have used a simple trapezoidal integration method. Test calculations have shown that an increment of 10° is sufficiently accurate. Taking the equidistant coarse grid saves the computation time of the scattering integral to a very large extent, because much less grid points are required for the computation of the scattering integral than for the representation of the radiation field.

5.2.1. Zenith Angle Grid Optimization

[38] As a reference field for the grid optimization, the DOIT method is applied for an empty cloudbox using a very fine zenith angle grid. The interpolation error of the very fine zenith angle grid is assumed to be negligible. The grid optimization routine finds a reduced zenith angle grid which can represent the intensity field with the desired accuracy. It first takes the radiation at 0° and 180° and interpolates between these two points on all grid points contained in the fine zenith angle grid for all pressure levels. Then the differences between the reference radiation field and the interpolated field are calculated. The zenith angle grid point, where the difference is maximal is added to 0° and 180° . After that the radiation field is interpolated between these three points forming a part of the reduced grid and again the grid point with the maximum difference is added. Using this method, more and more grid points are added to the reduced grid until the maximum difference is below a requested accuracy limit.

[39] The top panel of Figure 4 shows the clear-sky radiation in all viewing directions for a sensor located at 13 km altitude. This result was obtained with a switched-off

cloudbox. The difference between the clear-sky part of the ARTS model and the scattering part is, that in the clear-sky part the radiative transfer calculations are done along the line of sight of the instrument whereas inside the cloudbox the RT calculations are done as described in the previous section to obtain the full radiation field inside the cloudbox. In the clear-sky part the radiation field is not interpolated, therefore we can take the clear-sky solution as the exact solution.

[40] The interpolation error is the relative difference between the exact clear-sky calculation (cloudbox switched off) and the clear-sky calculation with empty cloudbox. The bottom panels of Figure 4 show the interpolation errors for zenith angle grids optimized with three different accuracy limits (0.1%, 0.2% and 0.5%). The left plot shows the critical region close to 90° . For a grid optimization accuracy of 0.5% the interpolation error becomes very large, the maximum error is there about 8%. For grid accuracies of 0.2% and 0.1% the maximum interpolation errors are about 0.4% and 0.2% respectively. However for most angles it is below 0.2%, for all three cases. For down-looking directions from 100° to 180° the interpolation error is 0.14% for grid accuracies of 0.2% and 0.5%. Since the grid optimization method included exactly the same zenith angle grid points in this zenith angle range, the lines are exactly on top of each other. For a grid accuracy of 0.1% the interpolation error is below 0.2%. The interpolation errors can be larger than the grid accuracy because interpolations are performed repeatedly in each iteration, so that the errors due to interpolation possibly sum up.

5.2.2. Interpolation Methods

[41] Two different interpolation methods can be chosen in ARTS for the interpolation of the radiation field in the zenith angle dimension: linear interpolation or a three-point polynomial interpolation. The polynomial interpolation method produces more accurate results provided that the zenith angle grid is optimized appropriately. The linear interpolation method on the other hand is safer. If the zenith angle grid is not optimized for polynomial interpolation one should use the simpler linear interpolation method. Apart from the interpolation of the radiation field in the zenith angle dimension linear interpolation is used everywhere in the model. Figure 5 shows the interpolation errors for the different interpolation methods. Both calculations are performed on optimized zenith angle grids, for polynomial interpolation 65 grid points were required to achieve an accuracy of 0.1% and for linear interpolation 101 points were necessary to achieve the same accuracy. In the region about 90° the interpolation errors are below 1.2% for linear interpolation and below 0.2% for polynomial interpolation. For the other down-looking directions the differences are below 0.08% for linear and below 0.02% for polynomial interpolation. It is obvious that polynomial interpolation gives more accurate results. Another advantage is, that the calculation is faster because less grid points are required, although the polynomial interpolation method itself is slower than the linear interpolation method. Nevertheless, we have implemented the polynomial interpolation method so far only in the 1-D model. In the 3-D model, the grid optimization needs to be done over the whole cloudbox, where it is not obvious that one can save grid points. Applying the polynomial interpolation method using non-

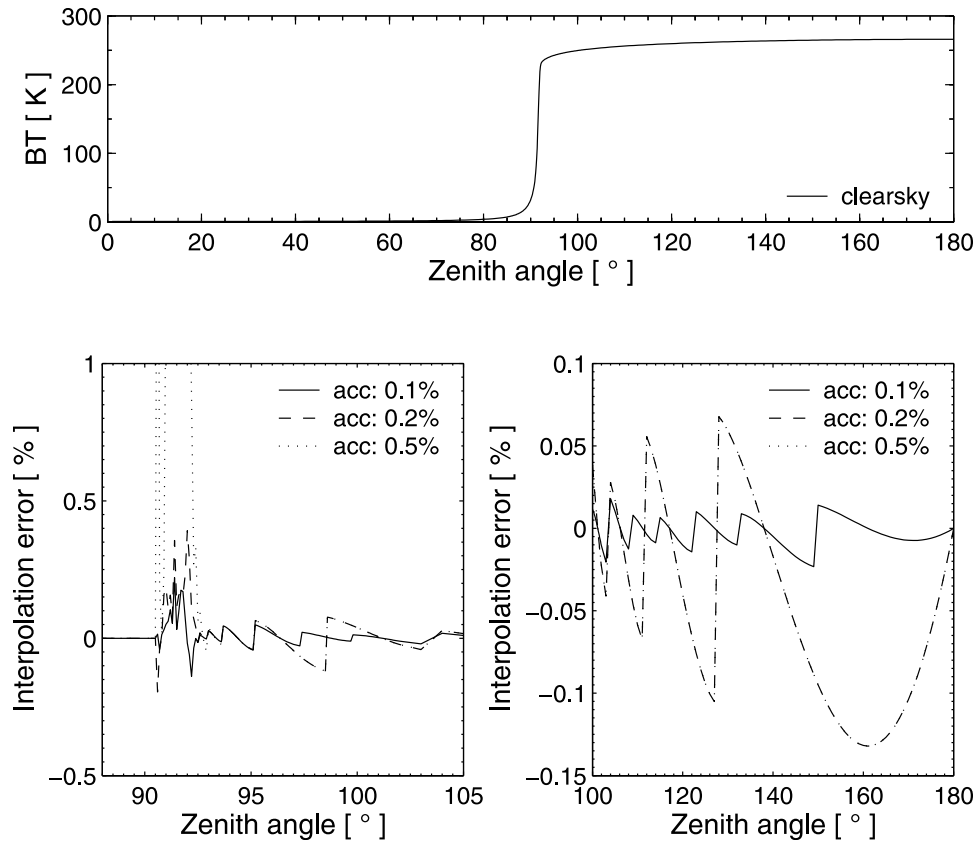


Figure 4. Interpolation errors for different grid accuracies. (top) Clear-sky radiation simulated for a sensor at an altitude of 13 km for all viewing directions. (bottom left) Grid optimization accuracy for limb directions. (bottom right) Grid optimization accuracy for down-looking directions.

optimized grids can yield much larger interpolation errors than the linear interpolation method.

5.2.3. Error Estimates

[42] The interpolation error for scattering calculations can be estimated by comparison of a scattering calculation performed on a very fine zenith angle grid (resolution 0.001° from 80° to 100°) with a scattering calculation performed on an optimized zenith angle grid with 0.1% accuracy. The interpolation error of the very fine zenith

angle grid is assumed to be negligible. The cloudbox used in previous test calculations is filled with spheroidal particles with an aspect ratio of 0.5 from 10 to 12 km altitude. The ice mass content is assumed to be $4.3 \cdot 10^{-3} \text{ g/m}^3$ at all pressure levels. We assumed an equal volume sphere radius of $75 \text{ }\mu\text{m}$. The particles are either completely randomly oriented (p20) or horizontally aligned with random azimuthal orientation (p30) (see Appendix B). The top panels of Figure 6 show the interpolation errors of the intensity.

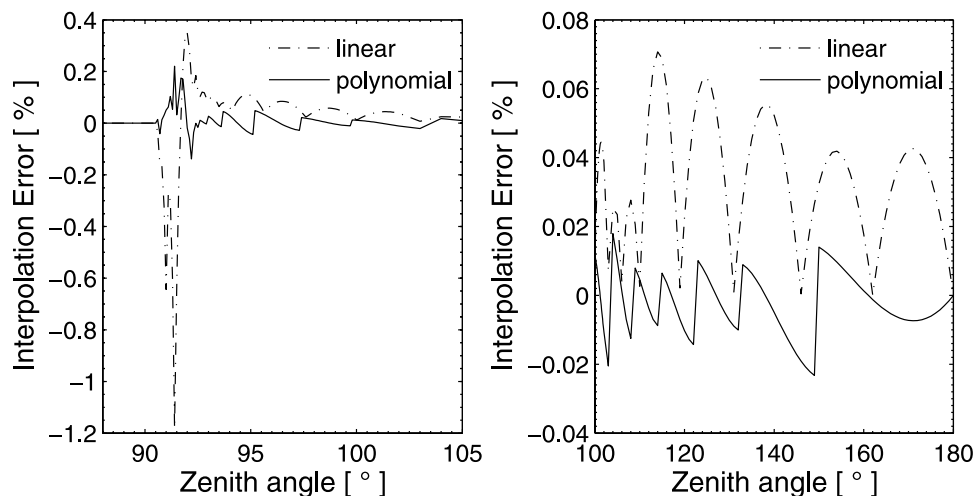


Figure 5. Interpolation errors for polynomial and linear interpolation.

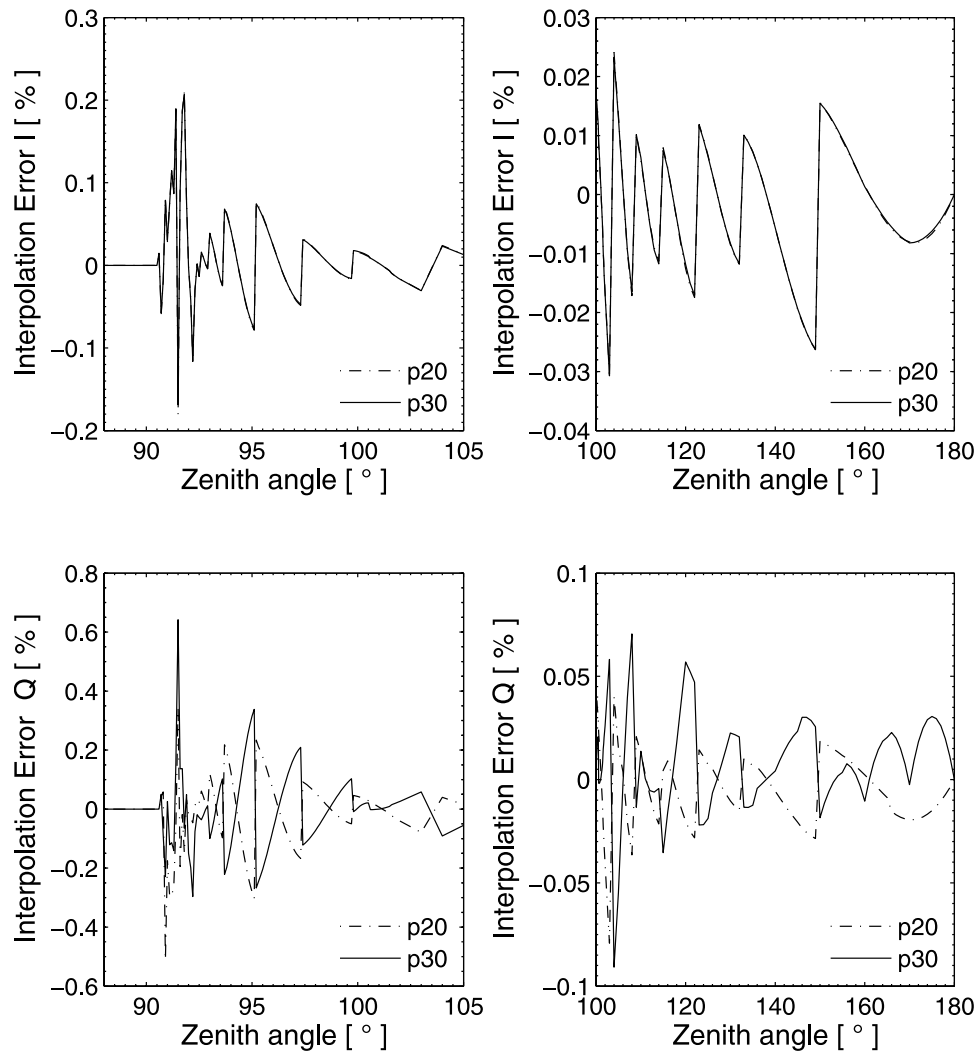


Figure 6. Interpolation errors for a scattering calculation. (left) Interpolation errors for limb directions. (right) Interpolation errors for down-looking directions. (top) Intensity I and (bottom) polarization difference Q .

For both particle orientations the interpolation error is in the same range as the error for the clear-sky calculation, below 0.2%. The bottom panels show the interpolation errors for Q . For the randomly oriented particles the error is below 0.5% and for the horizontally aligned particles with random azimuthal orientation it is below 0.7%. The maximum errors appear at zenith angles about 91.5° . It is obvious that the interpolation error for Q must be larger than that for I because the grid optimization is accomplished using only the clear-sky field, where the polarization is zero. Only the limb directions about 90° are problematic, for other down-looking directions the interpolation error is below 0.1%.

6. Model Simulations in a 1-D Spherical Atmosphere

[43] In all simulations it was assumed that the model atmosphere consists of nitrogen and oxygen, and the two major atmospheric trace gases: water vapor and ozone. The concentrations are taken from FASCOD [Anderson et al., 1986] data for midlatitudes in summer and gas absorption

was calculated based on the HITRAN [Rothman et al., 1998] molecular spectroscopic database using the ARTS model (version 1.0). Atmospheric refraction was neglected here, but it could be considered as it is implemented. All calculations are carried out for 318 GHz. The results of the calculations are summarized in Table 1.

6.1. Scattering and Polarization Signal for Different Particle Sizes

[44] In order to study the impact of particle size on the radiation field, 1-D calculations were carried out for four different particle sizes (equal volume sphere radius): $25\ \mu\text{m}$, $50\ \mu\text{m}$, $75\ \mu\text{m}$ and $100\ \mu\text{m}$. As in the calculation for estimating the interpolation error, the particles are prolate spheroids with an aspect ratio of 0.5. They are either completely randomly oriented or horizontally aligned with random azimuthal orientation. The cloud altitude is 10–12 km and the ice mass content is $4.3 \cdot 10^{-3}\ \text{g/m}^3$, which is rather small. The small value is used in order to compensate for the fact that the 1-D model assumes a cloud with infinite horizontal extent. Figure 7 shows the radiation field just

Table 1. Summary of Simulations

Size, μm	Aspect Ratio	BT Enhancement		BT Depression		Polarization
		$\Delta\text{BT}_{\text{max}}$, K	$\Delta\text{BT}_{\text{min}}$, K	$\Delta\text{BT}_{120^\circ}$, K	Q_{max} , K	Q_{120° , K
<i>p20: Completely Randomly Oriented Particles</i>						
25	0.5	7.56	-0.49	-0.04	-0.03	-0.00
50		11.67	-2.61	-0.23	-0.19	-0.00
75		21.32	-8.72	-0.75	-0.54	-0.01
100		35.04	-19.63	-1.72	-0.96	-0.01
75	0.5	21.32	-8.72	-0.75	-0.54	-0.01
	1.0	20.18	-8.21	-0.70	-0.53	-0.01
	2.0	21.45	-8.78	-0.76	-0.55	-0.01
<i>p30: Horizontally Aligned Particles With Random Azimuthal Orientation</i>						
25	0.5	7.11	-0.47	-0.04	-1.31	0.01
50		10.88	-2.47	-0.23	-2.13	0.03
75		19.65	-8.18	-0.75	-4.01	0.12
100		32.03	-18.29	-1.73	-6.33	0.32
75	0.5	19.65	-8.18	-0.75	-4.01	0.12
	1.0	19.82	-8.36	-0.71	-0.52	-0.01
	2.0	18.79	-7.78	-0.75	-6.42	0.20

above the cloud at 13 km altitude for completely randomly oriented particles. The scattering signal increases significantly with the particle size. The top panels show the difference between the scattered intensity field and the clear-sky field. About 90° two different features can be observed: a brightness temperature (BT) enhancement or a BT depression. The physical explanation is that the main source of radiation is the thermal radiation from the lower atmosphere. For zenith angles just above 90° there is a BT enhancement because radiation coming from the lower atmosphere is scattered inside the cloud into the limb directions. This part of the radiation is missing in the down-looking directions, therefore there is a BT depression for down-looking directions. The strongest scattering signal is observed in limb directions, as here the path-length through the cloud is the largest. The bottom panels of Figure 7 show the polarization signal, which is very small for randomly oriented particles. The largest polarization is observed for the largest particles ($R = 100 \mu\text{m}$) at about 91.5° , but even in this case it is below 1 K. The discrete jumps for zenith angles from 100° to 180° result from the polynomial interpolation of the radiation field on the cloud-box boundary, which is taken as radiative background for a clear-sky calculation toward the sensor. This interpolation is necessary since the intersection zenith angle of the line of sight of the sensor with the cloudbox boundary is not necessarily contained in the optimized zenith angle grid, which is used for the representation of the radiation field. Since we use a three-point polynomial interpolation scheme, these jumps occur where we use a different set of three points for the interpolation. The resolution of the optimized zenith angle grid is much coarser for angles close to nadir because the radiation field does not change rapidly here. The absolute value of the jumps is very small, they can only be seen so clearly, since the scattering signal for nadir is also very small. The interpolation error is below 0.2% as shown in Figure 6.

[45] Figure 8 shows the equivalent plots for particles which are horizontally aligned with random azimuthal orientation. The intensity plots are similar to the cloud case with completely randomly oriented particles. The polarization signal is much larger for oriented particles. The maximum polarization difference (Q equals the vertical minus the horizontal intensity component) is -6.3 K for the largest

particles. In most regions Q is positive (partial vertical polarization), only in limb-directions just above 90° it is negative (partial horizontal polarization). The sign of the polarization signal is determined by two opposing mechanisms: dichroism, as manifested by a nondiagonal extinction matrix; and the effect of radiation being scattered into the line of sight. For angles just above 90° the radiation being scattered into the line of sight is the dominating mechanism, which results in a negative Q . For down-looking directions, where the cloud is between the main radiation source and the sensor the dichroism effect is dominating, which results in a positive Q . The figure shows that polarization is very significant for limb radiances when the particles are oriented.

6.2. Effect of Particle Shape

[46] In order to look at the effect of particle shape, simulations were carried out for particles with aspect ratios 0.5 (prolate spheroids), 1.0 (spheres) and 2.0 (oblate spheroids). The particle size was $75 \mu\text{m}$ for all calculations and ice mass content and cloud height were the same as in the previous calculations. Figure 9 shows the results for completely randomly oriented particles. The radiation field does not change significantly for different aspect ratios. This means that the particle shape is not important for this particular setup. Figure 10 shows the equivalent simulations for horizontally aligned particles with random azimuthal orientation. Here there are significant differences between the different particle shapes. The intensity plots show that the BT enhancement and the BT depression are similar for all particle shapes (see Table 1). The maximum value of Q is -6.4 K and -4.0 K for oblate spheroids and prolate spheroids, respectively. For spherical particles there is only a very small polarization signal. More simulations are required to study in detail the effect of particle shape on the polarization signal.

6.3. Scalar Simulations

[47] In order to save CPU time and memory one can use the scalar version of the model (see section 3.3). To test the accuracy of the scalar approximation, all calculations presented above were performed using the scalar version. Figure 11 shows the differences between the scalar and the vector calculations for completely randomly oriented

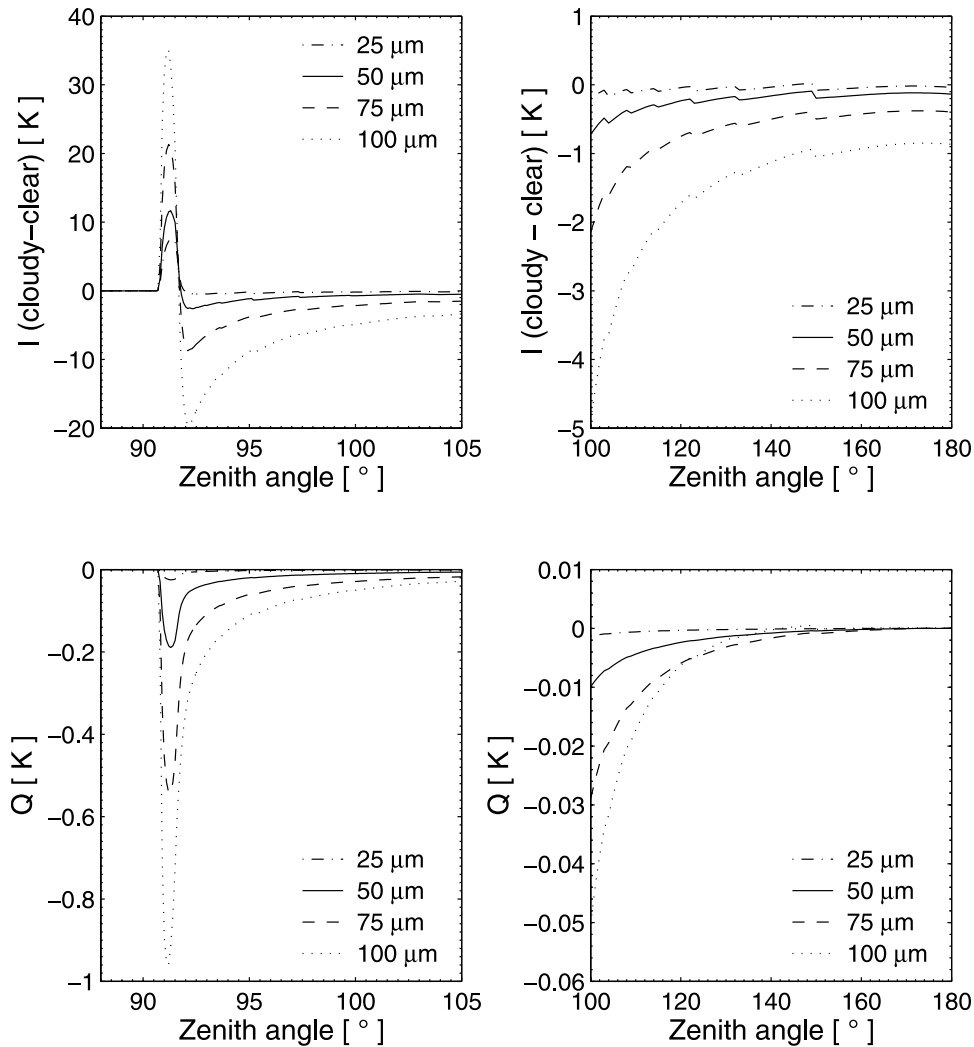


Figure 7. Scattering signal of completely randomly oriented particles with effective particle sizes 25 μm, 50 μm, 75 μm, and 100 μm for 318 GHz at 13 km altitude. (top) Intensity difference between scattering calculation and clear-sky calculation. (bottom) Difference between horizontal and vertical polarization.

particles with different effective radii. The maximum difference for limb directions is 0.01 K and for down-looking directions $7 \cdot 10^{-4}$ K. These small differences show, that it is not necessary to use the fully polarized vector version to model the radiative transfer through scattering media with completely randomly oriented particles. The previous section has also shown, that the polarization signal is negligible for such cases. Figure 12 shows the equivalent results for horizontally aligned particles. For down-looking directions the difference is below 0.02 K but for limb-cases it can go up to 1.5 K. For this reason one should use the vector model for limb RT simulations through scattering media consisting of oriented particles even if one is only interested in the total intensity of the radiation.

7. Three-Dimensional Box Type Cloud Model Simulations

[48] The 3-D version of the model was applied for simulating limb radiances for a cloud of finite extent

embedded in a horizontally homogeneous atmosphere. The height of the cloudbox was 7.3 km to 12.5 km and the vertical extent of the cloud was from 9.4 km to 11.5 km. The latitude range was 0° to 0.576° and the longitude range was 0° to 0.288° . This corresponds to a horizontal extent of approximately 64×32 km. A coarse spatial discretization was chosen, because a fine resolution is not necessary when the cloud is homogeneous, the number of grid points was $6 \times 9 \times 5$. Simulations were performed for two different IMC: 0.02 g/m^3 and 0.1 g/m^3 corresponding to limb optical depths of approximately 0.5 and 2.8 respectively. The maximum propagation path step length was set to 1 km for the optically thin cloud and to 250 m for the optically thicker cloud. These values allow to assume single scattering for each propagation path step. It was assumed that the cloud consists of spheroidal ice particles with a particle size of 75 μm and an aspect ratio of 0.5. Calculations were performed for totally randomly oriented particles and for horizontally aligned particles with azimuthally random orientation. The sensor was placed on board a satellite

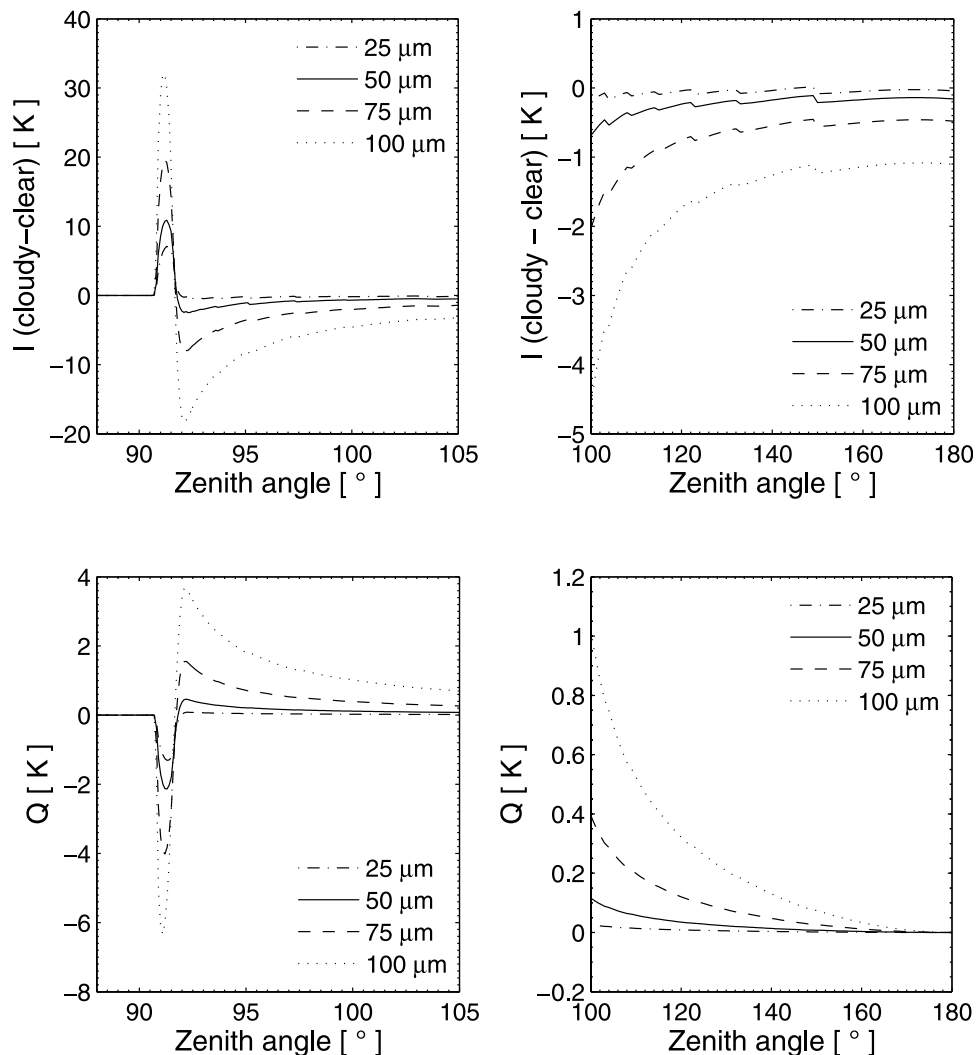


Figure 8. Scattering signal of horizontally aligned particles with effective particle sizes 25 μm , 50 μm , 75 μm , and 100 μm for 318 GHz at 13 km altitude. (top) Intensity difference between scattering calculation and clear-sky calculation. (bottom) Difference between horizontal and vertical polarization.

following a polar orbit at 820 km altitude. At each sensor position tangent altitudes from 0 to 13 km were measured. Figure 13 shows corresponding lines of sight (LOS). The figure shows that the cloud is seen from different sides, from the top, from the bottom or from the left side. When the satellite is at latitude 25° the cloud is only seen for low tangent altitudes (from 0 to 6 km). The cloud is seen at higher tangent altitudes at 27.5° . For even greater latitudes the sensor sees the cloud from the bottom. Note that the tangent point in the first plot is behind the cloud, in the second plot in the middle of the cloud and in the last plot in front of the cloud. In order to compare the 1-D and the 3-D model versions, simulations for a 1-D cloud layer with equivalent limb optical depths at 10 km tangent height were performed. The IMC for the equivalent 1-D clouds were 0.005 g/m^3 and 0.025 g/m^3 .

[49] Figure 14 shows the simulated radiances plotted as a function of tangent altitude and sensor position for totally randomly oriented particles. The top panels show the intensity differences between the clear-sky calculation and the cloudy-sky calculation. The bottom panels show the

polarization difference Q . The contour plots on the left hand side are the 3-D results. Reddish colors indicate a brightness temperature enhancement due to the cloud and bluish colors indicate a BT depression. White means that there is no cloud effect. A cloud effect can only be seen at tangent heights for which the corresponding LOS intersect with the cloud. The intensity plot shows that up to a latitude of 27° there is BT depression due to the cloud. The reason is that in those cases the tangent point, from where the major source of thermal radiation emerges, is behind the cloud. The cloud scatters part of the radiation away from the line of sight. For latitudes above 28° a BT enhancement is observed. In these cases the tangent point is in front of the cloud. The sensor measures all radiation emerging from the tangent point and additionally the back-scattered radiation from the cloud behind the tangent point. If the tangent point is inside the cloud, between 26.5° and 28° , a BT enhancement can be observed for high tangent altitudes because part of the upwelling radiation from the lower atmosphere is scattered into the direction of the LOS. For lower tangent points the scattering away from the LOS dominates, hence a BT

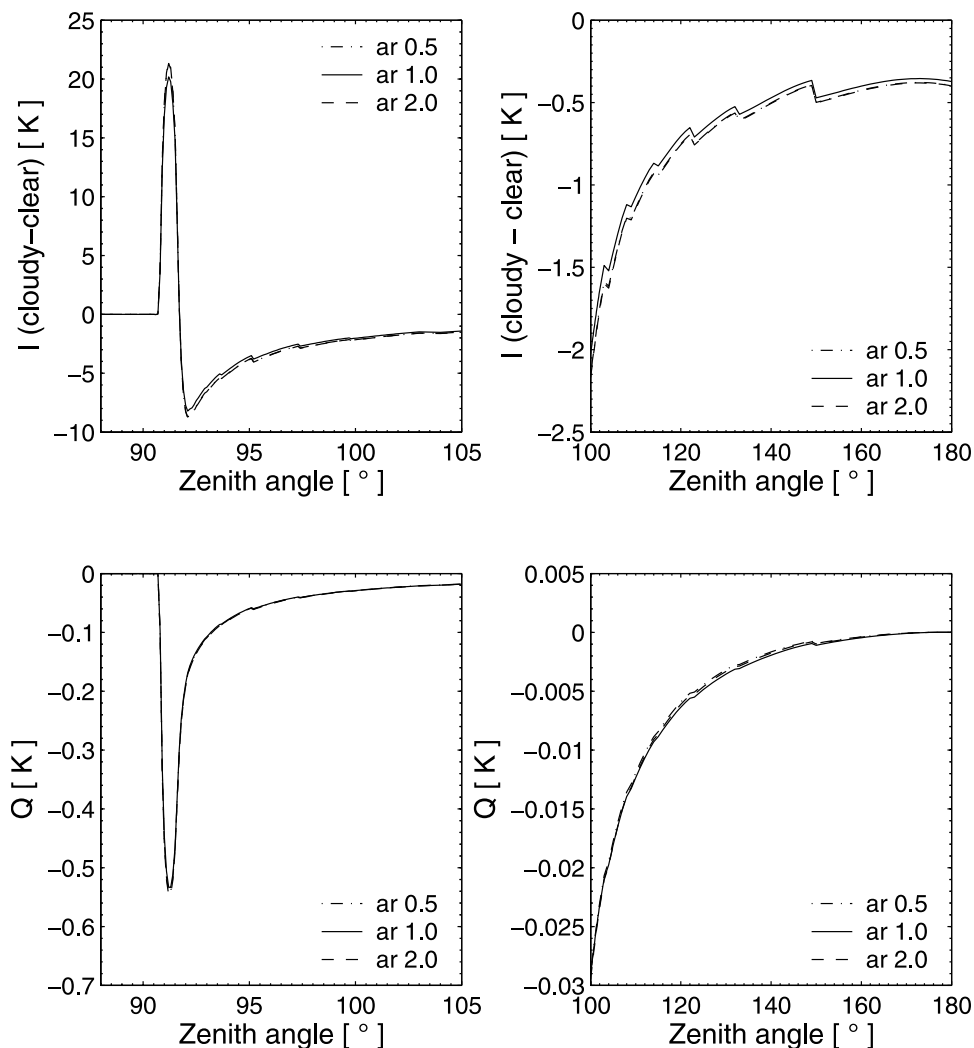


Figure 9. Scattering signal of completely randomly oriented spheroidal particles with aspect ratios 0.5, 1.0, and 2.0 for 318 GHz at 13 km altitude. (top) Intensity difference between scattering calculation and clear-sky calculation. (bottom) Difference between horizontal and vertical polarization.

depression is observed in this latitude range. The maximum absolute values for the BT enhancement and the BT depression are 19 K and -23 K respectively. The equivalent 1-D result on the right hand side shows a larger BT enhancement of 22 K and a smaller BT depression of -10 K. The BT depression is smaller because the optical depth for tangent heights below the cloud is smaller in the 1-D calculation compared to the 3-D calculation with much larger IMC. The polarization plots shows that in the 3-D case as well as in the 1-D case there is only a very small polarization difference for totally randomly oriented particles. In 3-D it is between -0.4 K and 0.1 K and for 1-D between -0.5 K and 0 K. In 1-D, only negative polarization is observed whereas in 3-D it can be positive or negative. The intensity plot in Figure 15 for azimuthally randomly oriented particles looks similar to that for completely randomly oriented particles. However, the maximum values of BT enhancement and BT depression are slightly smaller, about 17 K and -22 K, respectively. In 1-D the intensity differences are in the range of -9 K to 20 K. The polarization difference becomes much larger, between

-3.5 K and 4.0 K can be observed in the 3-D simulation and between -4.0 K and 1.7 K in the equivalent 1-D simulation.

[50] Figure 16 shows the results of the simulation for the thicker cloud consisting of horizontally aligned particles. The pattern looks very similar to that obtained for the thinner cloud but the absolute values of BT depression, BT enhancement and polarization are much larger. The intensity difference is in the range from -63 K to 45 K and the polarization difference is in the range from -7.0 K to 5.2 K for the 3-D calculation. The equivalent 1-D result ranges from -35 K to 55 K for the intensity and from -7.0 K to 5.2 K for the polarization difference. Since the pattern for the thicker cloud is similar to that obtained in the thin cloud case also for randomly oriented particles, we have not included the plot here. The intensity difference ranges in this case from -65 K to 47 K for 3-D and from -37 K to 58 K for 1-D. The polarization difference ranges from -0.7 K to 0.8 K for 3-D and from -1.0 K to 0 K for 1-D.

[51] Overall the comparison between 1-D and 3-D shows similar results at tangent heights inside the cloud, where the

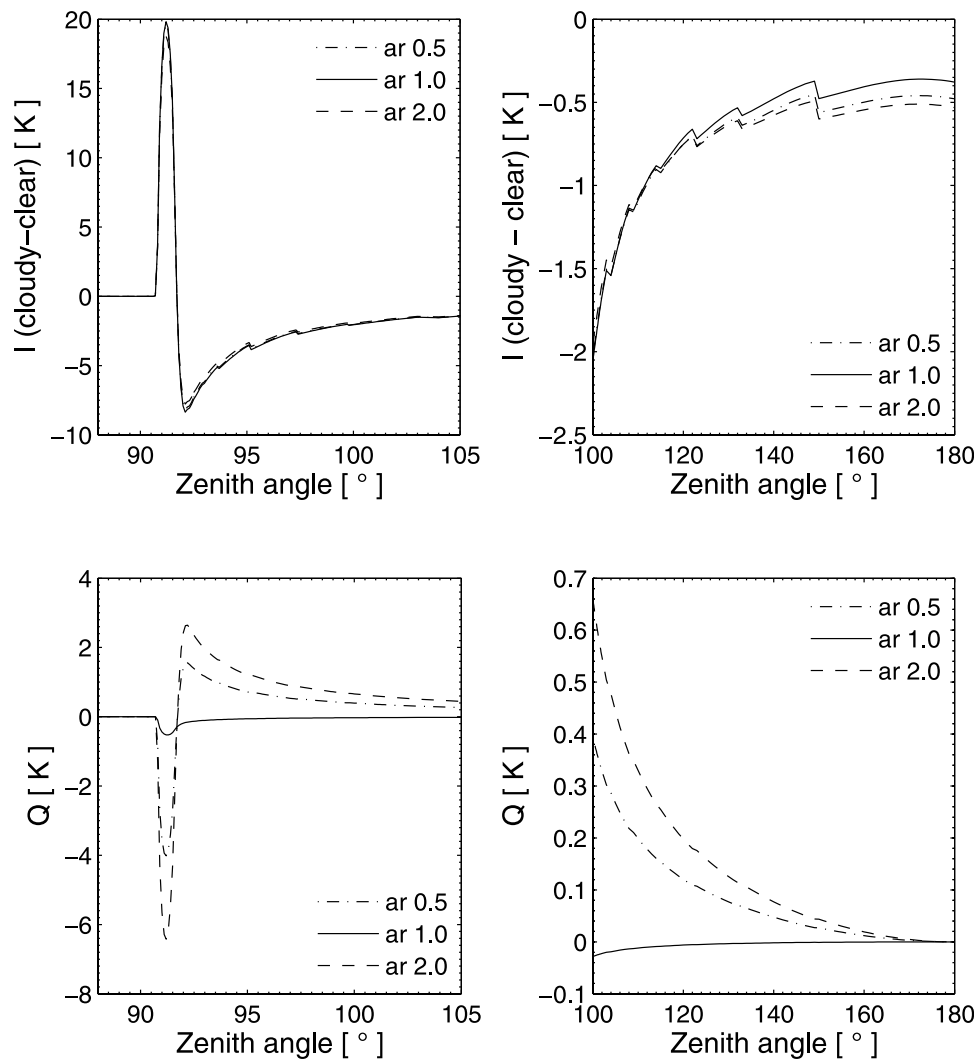


Figure 10. Scattering signal of horizontally aligned spheroidal particles with aspect ratios 0.5, 1.0, and 2.0 for 318 GHz at 13 km altitude. (top) Intensity difference between scattering calculation and clear-sky calculation. (bottom) Difference between horizontal and vertical polarization.

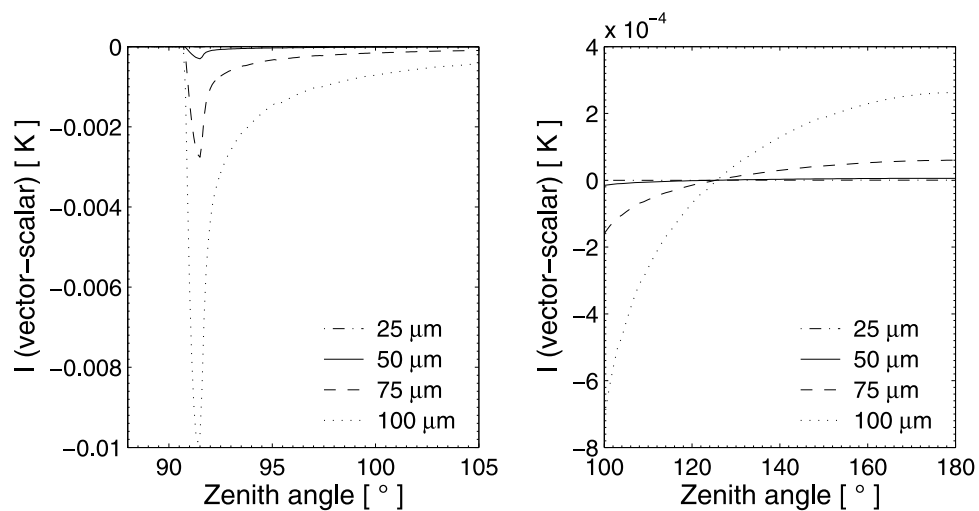


Figure 11. Difference between vector RT and scalar RT calculations for completely randomly oriented spheroidal particles (aspect ratio 2.0) for 318 GHz at 13 km altitude.

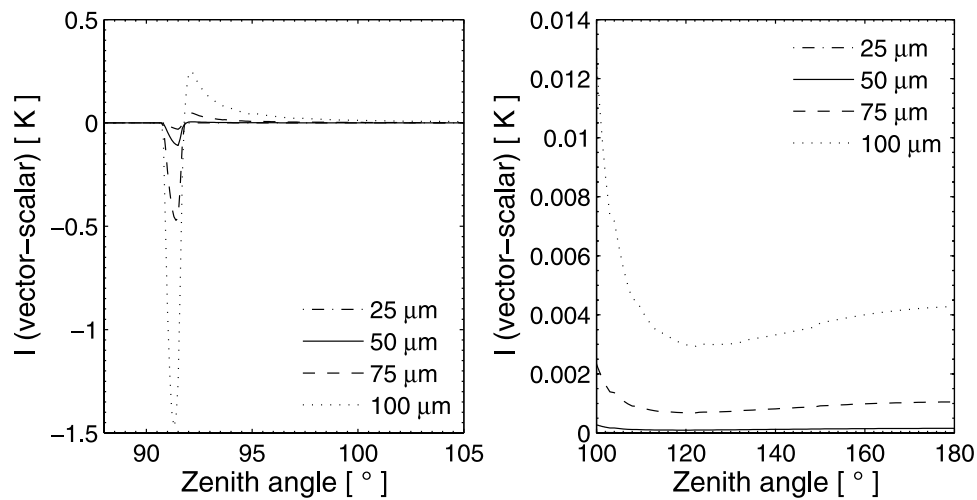


Figure 12. Difference between vector RT and scalar RT calculations for horizontally aligned spheroidal particles (aspect ratio 2.0) for 318 GHz at 13 km altitude.

optical depth is approximately equivalent. For other tangent heights, the optical depths are different and therefore the results deviate strongly. Moreover the scattering signal in 3-D depends very much on the sensor position w.r.t. the cloud. Hence it is very important to use the 3-D model where the cloud extent is not very large, like in this example case, or where the clouds are horizontally inhomogeneous.

[52] The CPU time for the thin cloud cases was approximately 50 min on a 3 GHz Pentium 4 processor, when all four Stokes components were calculated. U and V are not discussed as they are approximately zero (less than 10^{-7} K) for all calculations. The computation time can be reduced by 25% without losing accuracy when one runs the model only for two Stokes components. The computation time for

the same scenario was in this case approximately 37 min. The calculation for the thicker cloud took much longer, because the maximum propagation-path step length needed to be reduced. The calculation for all four Stokes components took approximately 150 min.

[53] The computation time increases strongly with the size of the cloudbox. Doubling the number of grid points in 1-D means a doubling of the computation time. Therefore the 3-D version of the model can be used for accurate simulations to study the effect of cloud inhomogeneity, but it is not applicable for operational use. The performance of the 1-D version of the model is much better. All 1-D simulations shown in this paper needed less than 30 s CPU time. The 1-D version of the model can therefore also be applied to

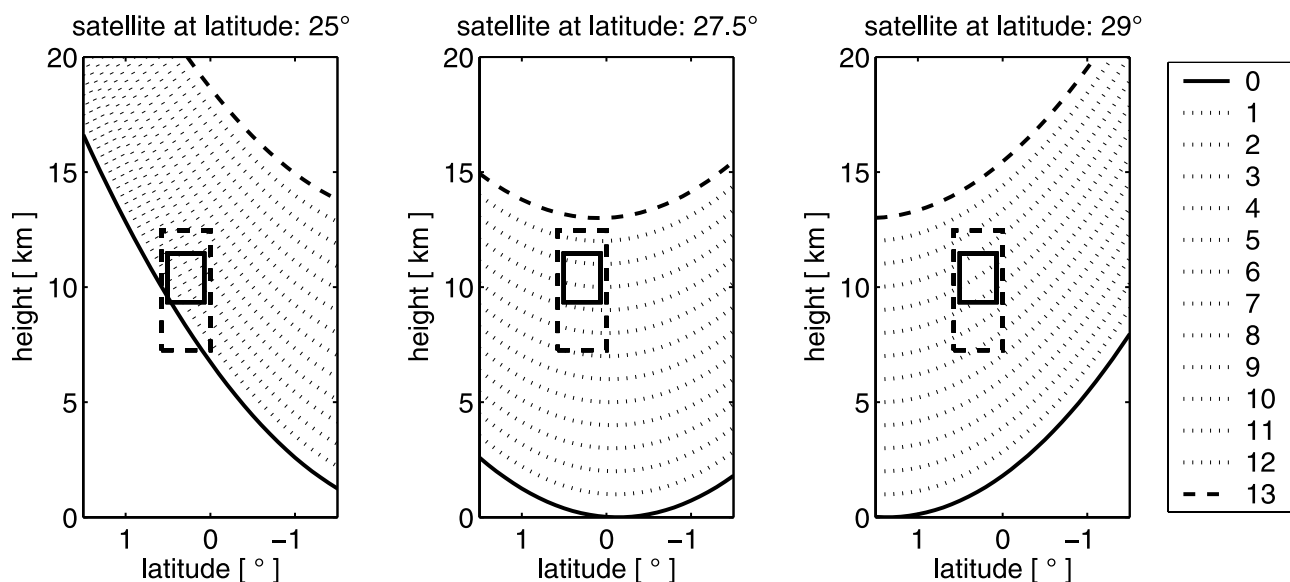


Figure 13. Lines of sight (LOS) for different sensor positions and tangent altitudes (km). The solid line corresponds to a LOS for a tangent altitude of 0 km, and the dashed line corresponds to a LOS for a tangent altitude of 13 km. Dotted lines correspond to LOS for tangent heights between 0 and 13 km. Inside the solid rectangle the single scattering properties are defined, and the dashed rectangle labels the cloudbox.

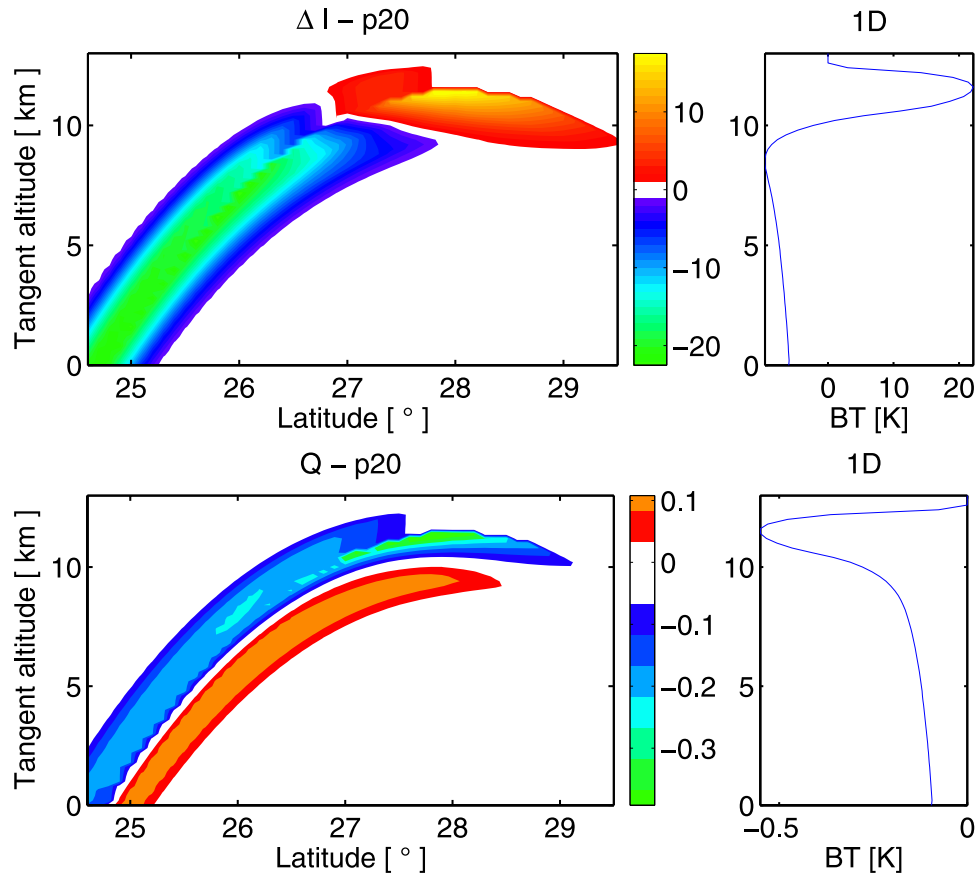


Figure 14. (left) Scattering signal of a 3-D box-type cloud embedded in a 1-D atmosphere as a function of sensor position and tangent altitude for 318 GHz. The cloud consists of completely randomly oriented spheroidal particles with a size of $75 \mu\text{m}$ and with an aspect ratio of 0.5. The IMC is 0.02 g/m^3 . (right) One-dimensional result for a cloud with an equivalent ice water path in limb (IMC = 0.005 g/m^3). The top plots show the intensity I , and the bottom plots show the polarization difference Q .

calculate full frequency spectra, for example to simulate the scattering effect of cirrus on the EOS MLS instrument.

8. Conclusions

[54] The Discrete Ordinate Iterative (DOIT) method has been implemented in the ARTS software package and applied for polarized radiative transfer calculations in the microwave spectral region.

[55] The DOIT algorithm solves the VRTE on a restricted part of the atmosphere denoted as the “cloudbox.” The scattering integrals for all discrete cloudbox points are first calculated using the clear-sky field. After that the VRTE is solved using a fixed term for the scattering integral. This yields the first iteration radiation field. Scattering integral fields and radiation fields are calculated alternately until convergence is obtained. In this way the VRTE is solved numerically for the cloudbox domain. The originality of the algorithm is the spherical geometry of the cloudbox, which is essential to perform simulations for limb sounding. The spherical geometry required numerical optimizations, for instance the zenith angle grid optimization for the representation of the radiation field.

[56] The example simulations have shown that the effect of particle size is very significant on both intensity and

polarization of the radiation. Particle shape is an important cloud parameter when the cloud particles are horizontally aligned with random azimuthal orientation. In the case of totally randomly oriented particles, changing the particle shape shows almost no effect in the simulations. For horizontally aligned particles, there is a significant difference between the scalar (unpolarized) version and the vector (polarized) version of the model in intensity. Therefore it is important to use a vector radiative transfer model to obtain accurate results, even if one is only interested in intensity, not in polarization. The 3-D simulations show that one must not neglect cloud inhomogeneity effects. The scattering signal depends very much upon the sensor position with respect to the cloud. The fact that the scattering signal is much larger in limb geometry compared to down-looking geometries, due to the greater path-length through the cloud layers, demonstrates the potential of retrieving cloud properties from limb measurements.

[57] ARTS is a modular program and can be run in different modes. Computation (CPU) time depends very much upon the chosen setup, whether one uses the 1-D or the 3-D mode, or selects the polarized or the unpolarized mode. CPU time can also be reduced by calculating two instead of all four Stokes components. The accuracy of the results is not affected, as long as U and V are negligibly

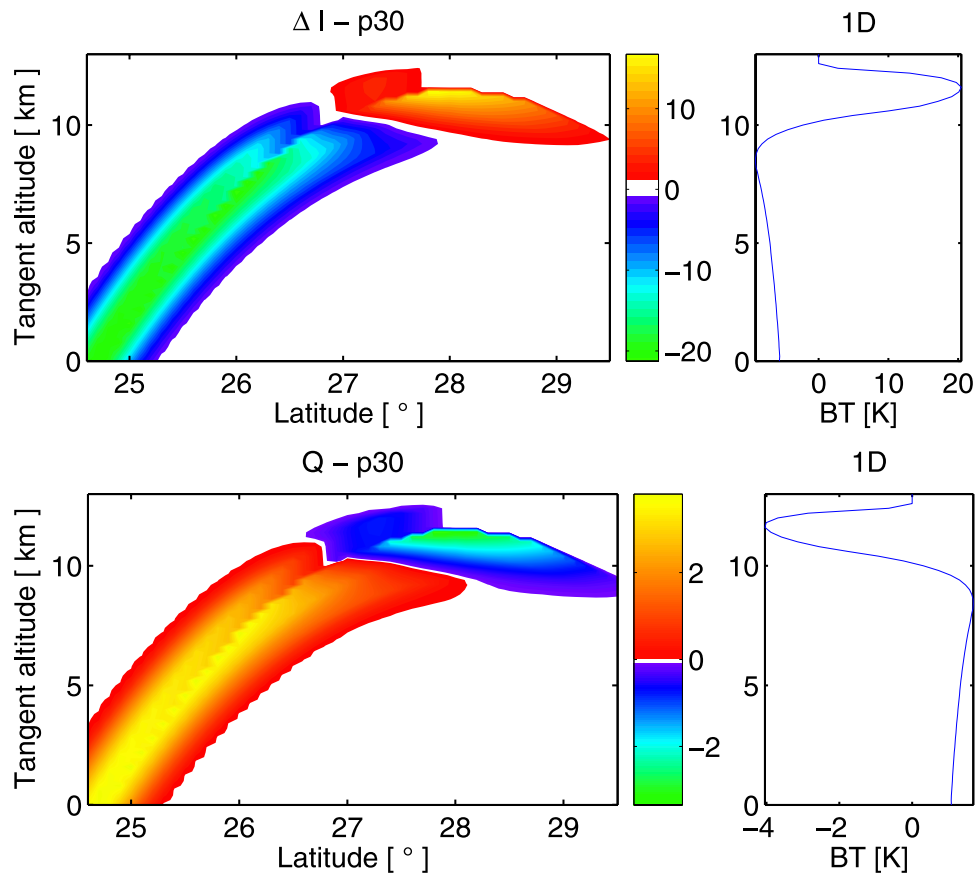


Figure 15. (left) Scattering signal of a 3-D box-type cloud embedded in a 1-D atmosphere as a function of sensor position and tangent altitude for 318 GHz. The cloud consists of horizontally aligned spheroidal particles with a size of $75 \mu\text{m}$ and with an aspect ratio of 0.5. The IMC is 0.02 g/m^3 . (right) One-dimensional result for a cloud with an equivalent ice water path in limb (IMC = 0.005 g/m^3). The top plots show the intensity I , and the bottom plots show the polarization difference Q .

small. Grid optimization is very important for both accuracy and computation time. Although the polarized calculations, especially in a 3-D atmosphere, are computationally demanding and therefore not yet useful for operational applications, the model is practical for research, for instance to study in detail the effect of different cloud parameters on polarization. A feature of the DOIT method is, that it yields the whole radiation field. To simulate radiances for different sensor positions, the radiation field only needs to be calculated once for the whole cloudbox and the outgoing radiances can then be interpolated on each required viewing direction. The ARTS package, which includes besides the scattering tools (Monte Carlo and DOIT) various functions for clear-sky radiative transfer and sensor modeling, is freely available under the Gnu General Public License and can be downloaded from <http://www.sat.uni-bremen.de/arts/>.

Appendix A: Solution of Approximated VRTE

[58] Equation (9) can be solved analytically using the following matrix exponential approach:

$$\mathbf{I}^{(1)} = e^{-\langle \mathbf{K} \rangle s} \mathbf{C}_1 + \mathbf{C}_2 \quad (\text{A1})$$

Here \mathbf{C}_1 and \mathbf{C}_2 are constants which have to be determined. Substituting (A1) into (9) gives the constant \mathbf{C}_2 :

$$\mathbf{C}_2 = \langle \mathbf{K} \rangle^{-1} \left(\langle \mathbf{a} \rangle \overline{\mathbf{B}} + \langle \mathbf{S}^{(0)} \rangle \right) \quad (\text{A2})$$

\mathbf{C}_1 can be determined using the initial condition, which is the radiation at the intersection point \mathbf{P}' traveling toward the observation point \mathbf{P} :

$$\mathbf{I}^{(1)}(s=0) = \mathbf{I}^{(0)}(\text{at intersection point}) \quad (\text{A3})$$

From ansatz:

$$\mathbf{C}_1 = \overline{\mathbf{I}^{(0)}} - \langle \mathbf{K} \rangle^{-1} \left(\langle \mathbf{a} \rangle \overline{\mathbf{B}} + \langle \mathbf{S}^{(0)} \rangle \right) \quad (\text{A4})$$

Substituting (A2) and (A4) into equation (A1) leads to the solution:

$$\mathbf{I}^{(1)} = e^{-\langle \mathbf{K} \rangle s} \mathbf{I}^{(0)} + \left(\mathbf{1} - e^{-\langle \mathbf{K} \rangle s} \right) \langle \mathbf{K} \rangle^{-1} \left(\langle \mathbf{a} \rangle \overline{\mathbf{B}} + \langle \mathbf{S}^{(0)} \rangle \right) \quad (\text{A5})$$

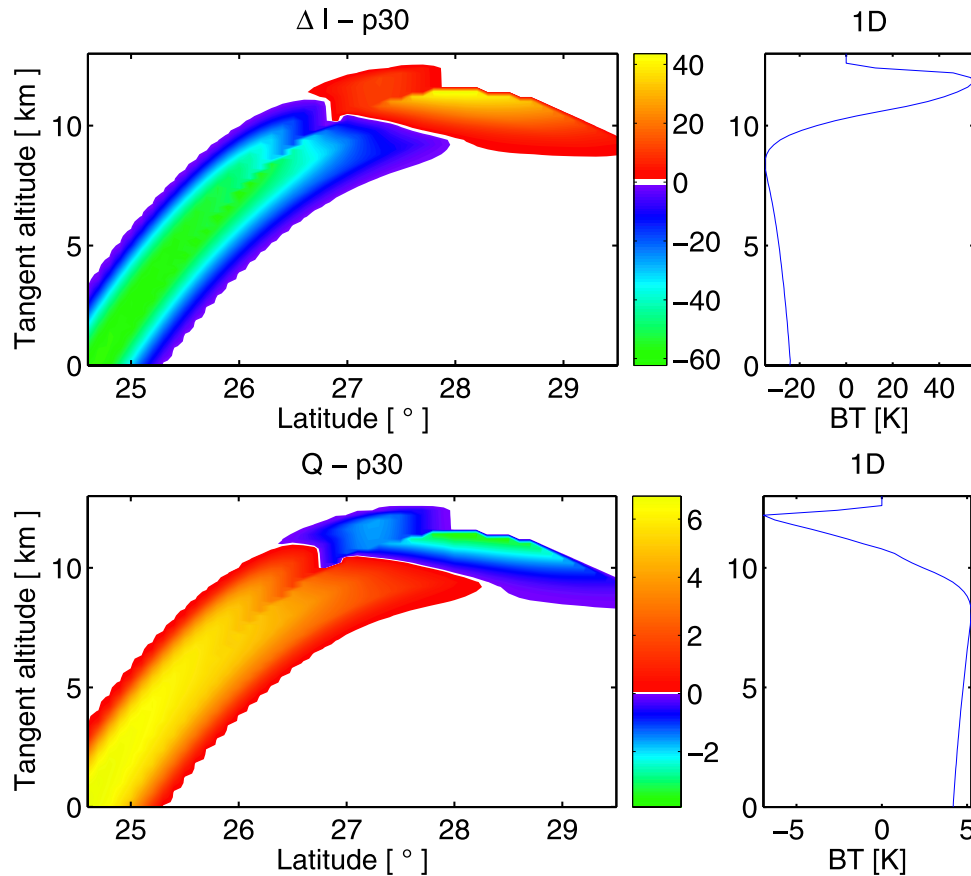


Figure 16. (left) Scattering signal of a 3-D box-type cloud embedded in a 1-D atmosphere as a function of sensor position and tangent altitude for 318 GHz. The cloud consists of horizontally aligned spheroidal particles with a size of $75 \mu\text{m}$ and with an aspect ratio of 0.5. The IMC is 0.1 g/m^3 . (right) One-dimensional result for a cloud with an equivalent ice water path in limb (IMC = 0.025 g/m^3). The top plots show the intensity I , and the bottom plots show the polarization difference Q .

[59] Here $\mathbf{1}$ denotes the identity matrix and $\mathbf{I}^{(0)}$ the Stokes vector at the intersection point. There are several ways to calculate the matrix exponential functions. In ARTS the Pade-approximation is implemented according to *Moler and Loan* [1979].

Appendix B: Database for Single Scattering Properties

[60] The radiative properties of cloud particles are described by emission, absorption and scattering (see equation (1)). The calculation of these properties can be computationally demanding, depending on the shape of the particles. For spherical particles one can use the analytical Mie theory. However, realistic cirrus clouds consist of different kinds of particles of various shapes. The asymmetrical particle shape leads to polarization of the scattered radiation, therefore it is necessary to be able to handle also aspherical shapes. In ARTS the single scattering properties are precalculated, for example, using the PyARTS package, which combines the T-matrix method as implemented by Mishchenko and a code for the computation of the refractive index of ice by *Warren* [1984]. The PyARTS package is freely available from [http://www.](http://www.met.ed.ac.uk/cory/PyARTS)

[met.ed.ac.uk/cory/PyARTS](http://www.met.ed.ac.uk/cory/PyARTS). The data are stored in XML-formatted files. The structure of the data files is shown in Table B1.

[61] It is possible to use the symmetry of the scattering medium to reduce the required storage memory for the single scattering properties. Four different particle types are implemented in ARTS:

[62] General case (p10): If there are no symmetries all sixteen elements of the phase matrix have to be stored for all frequencies and combinations of incoming and scattered directions. The individual phase matrices are calculated using Mishchenko's T-matrix code for single particles in fixed orientation [*Mishchenko*, 2000]. The extinction matrix has in general seven independent elements and the absorption vector has four elements.

[63] Macroscopically isotropic and mirror-symmetric scattering media (p20): In this case the particles are completely randomly oriented and the scattering properties are calculated in the particle frame. Using this coordinate system, only the scattering angle, which is the angle between incident and scattered direction, is needed instead of the four angles required in the general case. Furthermore the number of independent elements of both, phase matrix and extinction matrix, is reduced. Only

Table B1. Structure of Single Scattering Data Files

Symbol	Type	Dimensions	Description
	enum		specification of particle type
	string		short description of particle type
ν	vector	(ν)	frequency grid
T	vector	(T)	temperature grid
θ	vector	(θ)	zenith angle grid ($0^\circ \leq \theta \leq 180^\circ$)
ϕ	vector	(ϕ)	azimuth angle grid ($0^\circ \leq \phi \leq 180^\circ$)
$\langle \mathbf{Z} \rangle$	7D array	($\nu, T, \theta, \phi, \theta', \phi', i^a$)	phase matrix
$\langle \mathbf{K} \rangle$	5D array	($\nu, T, \theta, \phi, i^a$)	extinction matrix
$\langle \mathbf{a} \rangle$	5D array	($\nu, T, \theta, \phi, i^a$)	absorption vector

^aHere i is the matrix/vector element.

six elements of the phase matrix are independent. The extinction matrix is diagonal, therefore only one element needs to be stored in the data-files. The same is valid for the absorption vector. Moreover, extinction and absorption are independent of the propagation direction. To calculate the single scattering properties, Mishchenko's T-matrix code for randomly oriented particles [Mishchenko and Travis, 1998] is used. The transformations of the phase matrix from the scattering frame into the ARTS coordinate system are based on Mishchenko et al. [2002, chapter 4].

[64] Horizontally aligned plates and columns (p30): For particles that are azimuthally randomly oriented, one angular dimension of the phase matrix data array is redundant, as the phase matrix is independent of the incident azimuth angle. Furthermore, regarding the symmetry of this case, it can be shown that for the scattered directions only half of the angular grids are required. As for the general case, the fixed orientation T-matrix code for single scattering particles is used. The averaging over azimuthal orientations is done using the exact T-matrix averaging method of Mishchenko et al. [2000] for the extinction matrix, and by numerical integration for the phase matrix.

[65] Spherical particles (p40): In this case the single scattering properties are also calculated in the scattering frame. The number of independent phase matrix elements is only four. Extinction matrix and absorption vector are stored exactly in the same way as for the case of randomly oriented particles.

[66] **Acknowledgments.** We thank Oliver Lemke for programming assistance and technical support. Furthermore we thank Michael Mishchenko and Stephan Warren for making available the T-matrix program and the refractive index program, respectively. This study was funded by the German Federal Ministry of Education and Research (BMBF), within DLR project SMILES, grant 50 EE 9815, and within AFO2000 project UTH-MOS, grant 07ATC04. It was cofunded by ESA project UTLS, ESTEC contract 15457/02/NL/MW. It is a contribution to COST Action 723 "Data Exploitation and Modeling for the Upper Troposphere and Lower Stratosphere."

References

- Anderson, G. P., S. A. Clough, F. X. Kneizys, J. H. Chetwynd, and E. P. Shettle (1986), AFGL atmospheric constituent profiles (0–120 km), *AFGL Tech. Rep.*, TR-86-0110.
- Bohren, C., and D. R. Huffman (1998), *Absorption and Scattering of Light by Small Particles*, John Wiley, Hoboken, N. J.
- Buehler, S. A., P. Eriksson, T. Kuhn, A. von Engeln, and C. Verdes (2005), ARTS, the Atmospheric Radiative Transfer Simulator, *J. Quant. Spectrosc. Radiat. Transfer*, 91(1), 65–93, doi:10.1016/j.jqsrt.2004.05.051.

- Czekala, H., and C. Simmer (1998), Microwave radiative transfer with nonspherical precipitating hydrometeors, *J. Quant. Spectrosc. Radiat. Transfer*, 60(3), 365–374.
- Davis, C., C. Emde, and R. Harwood (2004), A 3D polarized reversed Monte Carlo radiative transfer model for mm and sub-mm passive remote sensing in cloudy atmospheres, *IEEE Trans. Geosci. Remote Sens.*, in press.
- Emde, C., S. A. Buehler, P. Eriksson, and T. R. Sreerexha (2004), The effect of cirrus clouds on microwave limb radiances, *J. Atmos. Res.*, doi:10.1016/j.atmosres.2004.03.023, in press.
- Eriksson, P., S. A. Buehler, C. Davis, C. Emde, T. R. Sreerexha, C. Melsheimer, and O. Lemke (2004), ARTS-1-1 user guide, Univ. of Bremen, Bremen, Germany. (Available at <http://www.sat.uni-bremen.de/arts/>)
- Evans, K. F. (1998), The spherical harmonics discrete ordinate method for three-dimensional atmospheric radiative transfer, *J. Atmos. Sci.*, 55, 429–466.
- Haferman, J. L., T. F. Smith, and W. F. Krajewski (1997), A multi-dimensional discrete-ordinates method for polarised radiative transfer. Part 1: Validation for randomly oriented axisymmetric particles, *J. Quant. Spectrosc. Radiat. Transfer*, 58, 379–398.
- Hartmann, G. K., et al. (1996), Measurements of O₃, H₂O, and ClO in the middle atmosphere using the Millimeter-wave Atmospheric Sounder (MAS), *Geophys. Res. Lett.*, 23(17), 2313–2316.
- Hoepfner, M., and C. Emde (2005), Comparison of single and multiple scattering approaches for the simulation of limb-emission observations in the mid-IR, *J. Quant. Spectrosc. Radiat. Transfer*, 91(3), 275–285, doi:10.1016/j.jqsrt.2004.05.066.
- Kerridge, B., et al. (2003), Consideration of mission studying chemistry of the UTLS, *Prog. Rep. 6*, Eur. Space Res. and Technol. Cent., Noordwijk, Netherlands.
- Kummerow, C. (1993), On the accuracy of the eddington approximation for radiative transfer in the microwave frequencies, *J. Geophys. Res.*, 98(D2), 2757–2765.
- Liu, Q., C. Simmer, and E. Ruprecht (1996), Three-dimensional radiative transfer effects of clouds in the microwave spectral range, *J. Geophys. Res.*, 101(D2), 4289–4298.
- Mishchenko, M. I. (2000), Calculation of the amplitude matrix for a nonspherical particle in a fixed orientation, *Appl. Opt.*, 39, 1026–1031.
- Mishchenko, M. I., and L. D. Travis (1998), Capabilities and limitations of a current FORTRAN implementation of the T-matrix method for randomly oriented rotationally symmetric scatterers, *J. Quant. Spectrosc. Radiat. Transfer*, 60, 309–324.
- Mishchenko, M. I., J. W. Hovenier, and L. D. Travis (Eds.) (2000), *Light Scattering by Nonspherical Particles*, Academic, San Diego, Calif.
- Mishchenko, M. I., L. D. Travis, and A. A. Lacis (2002), *Scattering, Absorption, and Emission of Light by Small Particles*, Cambridge Univ. Press, New York.
- Moler, C. B., and C. F. V. Loan (1979), Nineteen dubious ways to compute the exponential of a matrix, *SIAM Rev.*, 20, 801–836.
- Murtagh, D., et al. (2002), An overview of the Odin atmospheric mission, *Can. J. Phys.*, 80, 309–319.
- Roberti, L., J. Haferman, and C. Kummerow (1994), Microwave radiative transfer through horizontally inhomogeneous precipitating clouds, *J. Geophys. Res.*, 99(D8), 16,707–16,718.
- Rothman, L. S., et al. (1998), The HITRAN molecular spectroscopic database and HAWKS (HITRAN atmospheric workstation): 1996 edition, *J. Quant. Spectrosc. Radiat. Transfer*, 60, 665–710.
- Schulz, F. M., and K. Stamnes (2000), Angular distribution of the Stokes vector in a plane-parallel, vertically inhomogeneous medium in the vector

- discrete ordinate radiative transfer, *J. Quant. Spectrosc. Radiat. Transfer*, 65, 609–620.
- Simmer, C. (1993), Handbuch zu MWMOD, Kieler Strahlungstransportmodell fuer den Mikrowellenbereich, Inst. fuer Meereskunde, Kiel, Germany.
- Sreerekha, T. R., S. A. Buehler, and C. Emde (2002), A simple new radiative transfer model for simulating the effect of cirrus clouds in the microwave spectral region, *J. Quant. Spectrosc. Radiat. Transfer*, 75, 611–624.
- Warren, S. (1984), Optical constants of ice from the ultraviolet to the microwave, *Appl. Opt.*, 23, 1206–1225.
- Waters, J., et al. (1999), The UARS and EOS microwave limb sounder experiments, *J. Atmos. Sci.*, 56, 194–218.
-
- S. A. Buehler, C. Emde, T. R. Sreerekha, and C. Teichmann, Institute of Environmental Physics, University of Bremen, Otto-Hahn-Allee 1, D-28359 Bremen, Germany. (emde@uni-bremen.de)
- C. Davis, Institute for Atmospheric and Environmental Science, University of Edinburgh, Edinburgh EH9 3JZ, UK.
- P. Eriksson, Department of Radio and Space Science, Chalmers University of Technology, SE-41296 Göteborg, Sweden.